UCLouvain

epl

École polytechnique de Louvain

# Detection of linear light polarization with a diffuser camera

Author: **Lissa BERLO**
Supervisor: **Laurent JACQUES**
Readers: **Olivier LEBLANC, Marc GEORGES**
Academic year 2023–2024
Master [120] in Electro-mechanical Engineering

UNIVERSITÉ CATHOLIQUE DE LOUVAIN

ÉCOLE POLYTECHNIQUE DE LOUVAIN

# DETECTION OF LINEAR LIGHT POLARIZATION WITH A DIFFUSER CAMERA

AUTHOR

LISSA BERLO

SUPERVISOR

LAURENT JACQUES

READERS

OLIVIER LEBLANC

MARC GEORGES

UCLOUVAIN, JUNE 2024

# Abstract

Advancements in the observation of light polarization using innovative lensless imaging devices are widely explored in the scientific field. This Master's thesis studies the detection of linear light polarization using a lensless imaging device known as the DiffuserCam [3]. Light polarization detection holds significant promise across scientific domains, including biomedical imaging, materials mechanics, and remote sensing. By integrating linear polarizers into the DiffuserCam setup, this research aims to capture polarization data in a single instance. Thereby, it increases the efficiency and precision of polarization measurements while providing a low-cost, accessible, and compact system, unlike the current state-of-the-art. The study focuses on the reproduction of the DiffuserCam and the computation of Stokes parameters to detect and determine the orientation of linearly polarized light. The results underline the potential of the DiffuserCam in various applications involving the detection of light polarization due to its light and small design, accessible materials, and adaptability. Future directions include exploring advanced computational techniques for image reconstruction and error mitigation, as well as extending the system's capabilities to detect circular polarization, aiming to offer a full-stokes polarization lensless imaging system that is easily replicable and scalable.

# Acknowledgements

I would like to thank all those who supported me in any way during the writing of this Master's thesis,

My supervisor, Laurent Jacques, always understanding and ready to listen, who patiently gave me the tools I needed to complete my work, I am deeply grateful,

Olivier Leblanc, who also kindly guided me through certain parts and concepts with which I was less familiar,

François Wielant, who helped me with the design of the experimental setup, the loan of the necessary equipment, and the 3D printing of various parts, and who was very attentive to my needs during the *do-it-yourself* part of the project,

Souley Djadjandi, who helped me cut the polarizing filters and suggested several methods to move forward with my experiments,

Marc Georges, for agreeing to be on my jury,

And, of course, my family and my loved ones, who have supported me tirelessly and with kindness.

As part of the process of writing this dissertation,

I acknowledge the use of ChatGPT 3.5 (Open AI, chat.openai.com) for rephrasing sentences. I also used DeepL's tools in the preparation of this Master's Thesis, to translate text from French to English (DeepL Translator, deepl.com/translator), and paraphrase some sentences (DeepL Write, deepl.com/write).

Moreover, in the production of the Tikz image included in this work, I acknowledge that these images were created using code adapted from sources on tikz.net.

Throughout my research, GitHub Copilot (GitHub, docs.github.com/copilot) assisted me in writing, debugging, and optimizing code.

*This page intentionally left blank.*

# Contents

# Nomenclature

## Acronyms

| | |
|---|---|
| ADMM | Alternating Direction Method of Multipliers |
| AOLP | Angle of Linear Polarization |
| DMD | Digital Micromirror Device |
| DOLP | Degree of Linear Polarization |
| FISTA | Fast Iterative Shrinkage-Thresholding Algorithm |
| FoV | Field of View |
| FWHM | Full Width at Half Maximum |
| GD | Gradient Descent |
| LCD | Liquid Crystal Display |
| LCoS | Liquid Crystal on Silicon |
| LPIPS | Learned Perceptual Image Patch Similarity |
| LSI | Linear and Shift-Invariant |
| MAE | Mean Absolute Error |
| MSE | Mean Squared Error |
| PSF | Point Spread Function |
| PSNR | Peak Signal-to-Noise Ratio |
| RMSE | Root Mean Squared Error |
| SNR | Signal-to-Noise Ratio |
| SoC | Systems on Chips |
| SSIM | Structural Similarity Index |

## Symbols

| | |
|---|---|
| $\Delta$ | Phase shift in the Jones vector |
| $\Gamma$ | Intensities ratio matrix |
| $\hat{e}_{\pi/4}$ | Axis oriented at an angle of $\frac{\pi}{4} rad$ with $\hat{x}$ |
| $\hat{x}$ | Horizontal axis |
| $\hat{y}$ | Vertical axis |
| $\lambda$ | Wavelength |
| $\mathcal{F}$ | Fourier operator |
| $\mathcal{L}$ | Lagrangian operator |
| $\theta$ | Angle in the (x,y) plane |
| $\theta_{polarizer}$ | Polarizing filter orientation |
| $\theta_{source}$ | Incident light orientation |
| $\vec{E}$ | Electric field |
| $b$ | Captured signal |
| $d_f$ | Focal distance |
| $d_s$ | Source distance |
| $f$ | Downsampling factor |
| $h$ | Point Spread Function |
| $I$ | Intensity |
| $iters$ | Number of Iterations |
| $J$ | Jones vector |
| $L$ | Lipschitz constant |
| $Q$ | Intensity along the $\hat{e}_{\pi/4}$ axis coefficient |
| $Q$ | Intensity along the $\hat{x}$ axis coefficient |
| $R$ | R-coefficient for linear polarization detection |
| $R_\alpha$ | Rotation matrix |

| | |
|---|---|
| $S$ | Stokes parameters |
| $T$ | Jones Matrix |
| $v$ | Incident signal |
| $x$ | Position coordinate |
| $y$ | Position coordinate |
| $z$ | Position coordinate |

# List of Figures

# List of Tables

*This page intentionally left blank.*

# 1 Introduction

Polarization is a fundamental property of light that describes the orientation of the oscillations of light waves. Unlike other properties of light, such as intensity and wavelength, polarization reveals intricate details about how light interacts with its environment. This unique characteristic provides valuable insights into the source of the light and the medium through which it travels, making polarization detection a critical tool in various fields of science and technology.

In biomedical imaging, polarization can enhance contrast and reveal structural details of biological tissues that are invisible to conventional imaging techniques. This ability is crucial for identifying and diagnosing medical conditions with greater accuracy. As for the field of materials science, polarization analysis can characterize the optical properties of materials, leading to advances in manufacturing and quality control processes.

Traditional methods of polarization detection often involve complex and bulky optical setups, such as rotating polarizers or interferometers. These setups can be inconvenient and expensive, limiting their practical application, especially in portable or field-deployable systems. The need for more compact, cost-effective and versatile solutions has driven the search for innovative technologies.

Lensless imaging is a new technology that overcomes these limitations by replacing the traditional camera lens by computer processing and optical sensors. One of the lensless imaging systems, the DiffuserCam, uses a diffuser to scatter incoming light and computational algorithms to reconstruct three-dimensional images from the resulting light patterns. The DiffuserCam's ability to capture detailed images without lenses offers significant advantages in terms of size, cost and diversity.

This thesis explores the integration of linear polarizers into the DiffuserCam system to detect and analyze linear light polarization. By acquiring polarization information in a single shot, this approach aims to improve the efficiency and accuracy of polarization measurements. The study focuses on the analysis of Stokes parameters, which are

essential to recovering the orientation and degree of linear polarization. This research will develop a compact and adaptable system that increases our ability to detect and analyze the polarization of light, contributing to more efficient and versatile imaging technologies with a wide range of applications.

## Structure of the Master's thesis

This Master's thesis is structured in order to provide a complete investigation into the detection of linear polarization of light using a DiffuserCam. Following this introduction, the *Background* chapter reviews the existing research on light polarization detection and lensless imaging. It provides a critical analysis of previous studies.

The *Methodology* section details the experimental setup, including the integration of linear polarizers with the DiffuserCam, and outlines the procedures for acquiring and analyzing polarization data, along with the sources of error encountered. This is followed by the *DiffuserCam* chapter, where the implementation of this lensless imaging system is reproduced, explained and evaluated. Experimental results of the lensless polarization camera are presented and discussed in detail in Chapter 4. The *PolariCam* chapter highlights the effectiveness of the proposed method and addresses challenges such as filter attenuation. The *Discussion* chapter interprets the results in the context of the wider research landscape, explores the implications of the findings, and suggests potential improvements.

The main elements of this Master's thesis are finally summarized in the *Conclusion*. Furthermore, it opens the way for future research by raising further questions and improvements.

# 2

# Background and Methodology

This chapter develops the main concepts used in this Master's thesis. It provides a detailed overview of lensless imaging, a technology that is gradually replacing traditional imaging methods. It describes the background and explains the importance of light polarization. The chapter goes on to describe the methodology used to carry out this work and the potential sources of error that need to be addressed.

## 2.1 Lensless imaging

The basic principles of camera design have remained largely unchanged for centuries, dating back to early concepts by Ibn-al-Haytham [25] and Johann Zahn [26]. Traditional cameras typically consist of a box containing a lens that directs light onto a sensor, similar to the human eye. Despite advances in lens and sensor technology, the basic structure has endured. However, the emergence of new applications, such as wearables and IoT, requires the development of smaller, lighter cameras, prompting a re-evaluation of camera optics.

To meet this demand, lensless cameras replace conventional lenses with thin, low-cost optical encoders and computational algorithms for image reconstruction. This model belongs to the field of computational imaging, where hardware and software are designed together [10].

Lensless cameras offer many advantages:

- **Size**: They are extremely compact, some as thin as a millimeter.
- **Weight**: Their lightness is due to the absence of heavy lenses.
- **Cost**: They are economically advantageous, significantly reducing costs.
- **Scalability**: Using semiconductor manufacturing technologies, they are scalable.
- **Field of view**: They can achieve high resolution and a wide field of view.
- **Privacy**: Sensor data remains visually undetectable, enhancing privacy.

- **Compressive Imaging**: Capture more detailed images, including 3D and hyperspectral data, from fewer measurements.

However, lensless cameras have limitations:

- **Image quality**: Traditional lenses still deliver superior image quality.
- **Complexity**: Computational reconstruction introduces complexity, which can increase power consumption and processing time.
- **Light Collection**: The ability to collect light is limited by the size of the sensor, unlike conventional lenses, which can be larger to collect more light.

### 2.1.1 Main components of lensless cameras

Traditional lens-based cameras use a focusing lens to direct light from a scene onto an image sensor, creating a direct image. In contrast, lensless cameras use an optical modulator (such as a coded mask or diffuser) positioned close to the sensor to take indirect measurements. These measurements, although different from the final image, are processed computationally to reconstruct the image.

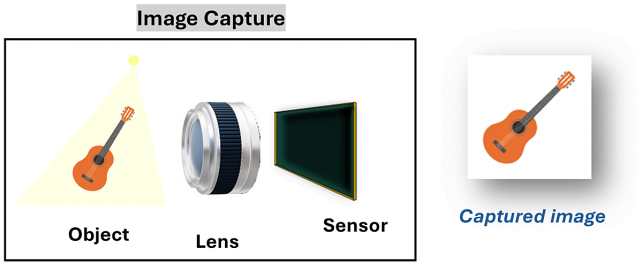


**Figure 2.1:** *Traditional lens-based imaging*

- **Sensor**: Typically uses CMOS or CCD arrays for visible light or specialized sensors for infrared imaging.
- **Modulator**: Optically encodes scene information using fixed masks (amplitude or phase) or programmable modulators such as spatial light modulators (SLMs).
- **Lighting**: Used to enhance image acquisition, it can include ambient, transillumination, off-chip side illumination, or on-chip integrated illumination methods.

The key points influencing the design of lensless cameras are the sensor-mask distance and the object distance. While the first one can be minimal, facilitating ultra-thin designs, the other influences the choice of illumination and resolution.

### 2.1.2 Categories of lensless cameras

Lensless cameras are categorized based on their modulation method [10].

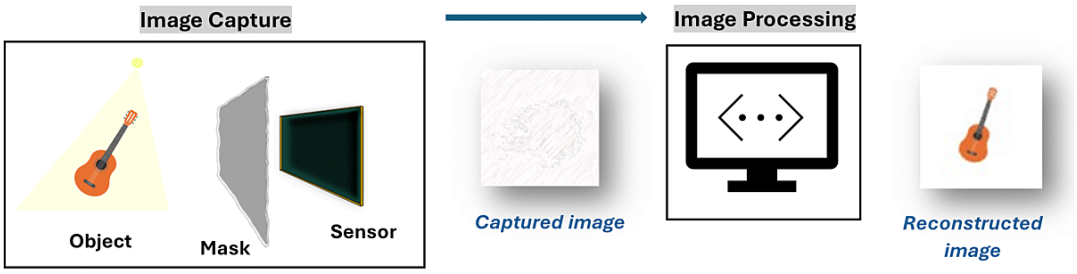


**Figure 2.2:** *Lensless imaging*

### Illumination-Modulated Systems

Illumination-modulated lensless systems utilize controlled lighting to capture various images for reconstruction:

- **Shadow Imaging**: This method employs constant illumination to generate shadow images, enhancing resolution through physical apertures or computational techniques. It is commonly used in lab-on-a-chip microscopy [23].
- **Holographic Imaging**: Holographic imaging utilizes coherent light to capture detailed diffraction patterns, enabling high-fidelity reconstruction [5]. It finds applications in analyzing biological samples such as blood cells and cancer tissues.
- **Time-Resolved Imaging**: This technique involves using pulsed light and time-resolved sensors to capture time-of-flight data [27]. However, it is limited by complex equipment and reconstruction methods.

### Mask-Modulated Systems

Mask-modulated lensless systems employ a fixed optical mask to modulate incoming light, creating versatile cameras suitable for various object distances and lighting conditions. These systems capture light patterns on a sensor, which are then decoded computationally to produce images [20].

In a mask-modulated system, the optical mask modulates the incoming light, shaping its intensity or phase distribution. When light passes through the mask and interacts with the object, it forms a light pattern on the sensor. This pattern, known as the PSF, represents how each point in the object space is spread out or blurred on the sensor plane.

The PSF encapsulates important information about the imaging system, including its resolution, aberrations, and spatial characteristics. Understanding and controlling the PSF are essential for reconstructing high-quality images from the sensor data in mask-modulated systems. By designing the optical mask and the system's computational algorithms to optimize specific PSF properties, such as sharpness and uniformity, researchers can enhance the system's imaging performance and capabilities.

Such systems are well represented in these examples:

- **FlatCam**: Utilizes a separable amplitude mask for thin cameras [4].
- **FlatScope**: A miniaturized design for 3D fluorescence microscopy [16].
- **DiffuserCam**: Uses a diffuser to create high-contrast PSFs for 2D and 3D imaging [3].

These systems offer versatility, compactness, and high-resolution imaging capabilities. However, amplitude masks have low light throughput, while phase masks can be expensive and complex to fabricate.

#### Programmable Modulated Systems

Programmable modulators, such as LCD, LCoS, and DMD, enable dynamic optical encoding for lensless cameras. This adaptability allows for capturing multiple lensless images, thereby enhancing reconstruction quality and reducing the required sensor pixels [28].

These systems offer improved reconstruction and flexibility in adapting to different imaging scenarios and object dynamics. However, the increased number of measurements may complicate reconstruction algorithms and limit the imaging of dynamic objects.

### 2.1.3 Image Reconstruction

The image reconstruction process in lensless cameras differs from traditional lens-based systems due to the absence of a lens. Instead, computational reconstruction is required to recover the scene intensity from sensor measurements. The process consists of calibration and measurements along with reconstruction algorithms. The often linear relation between sensor measurements $y$ and scene intensity $x$ is described by a forward model.

For 2D imaging, this model can be simplified using convolutional or separable approximations, significantly reducing the computational complexity. For 3D imaging, similar forward models can be extended to account for depth-dependent transfer functions. Light-field representations and holographic approaches offer alternative ways of extracting 3D information.

One important element for image reconstruction is the calibration of the imaging system. It is essential to accurately estimate model parameters, either through computational models or experimental measurements. Then, the reconstruction algorithms typically involve convex optimization to minimize the difference between measured and estimated data, while incorporating regularization to improve image quality. Data-driven techniques, particularly deep learning, have shown promise in improving reconstruction

accuracy by leveraging large data sets and learning complex patterns in the data.

These approaches enable the reconstruction of high-quality images from lensless camera measurements, with implications for applications as diverse as microscopy, surveillance and biomedical imaging.

### 2.1.4 Applications

In photography, lensless systems record scene details directly onto sensors, enabling features like comprehensive 2D imaging with consistent focus, the ability to adjust focus afterward, and even 3D imaging, especially effective for close-up shots. The work on the DiffuserCam [3] is one of the main photography applications that we describe later on in Chapter 3.

Microscopy can benefit from the compact nature of lensless imaging systems, offering wide Fields of View (FoV) and high resolution. However, challenges remain in achieving precise chromatic filtering, particularly in fluorescence mode such as in the FlatScope camera developed by Jesse K. Adams [16].

Emerging applications include lensless endoscopy and privacy-focused systems using holography imaging, like the work of Noam Badt and Ori Katz on holographic lensless micro-endoscopy [5].

Looking ahead, lensless imaging holds potential for applications limited by space, such as under-display cameras and micro-robotic vision, with the possibility of adaptable imaging surfaces. The efficiency of computational implementation is crucial, with potential solutions including wireless transmission of data and low-power processing Systems on Chips (SoCs).

Beyond imaging, lensless systems have potential for vision and inference applications, including but not limited to face detection and gesture recognition [24].

## 2.2 Light polarization

Light polarization is a fundamental property of light that describes the orientation of its oscillations. This property can be exploited in various imaging and sensing applications to gain additional information about a scene or material that is not available through intensity measurements alone [21].

### 2.2.1 Basics of Polarization

Polarization refers to the orientation of the oscillations of the electric field vector in a light wave. In unpolarized light, the oscillations occur in all possible directions perpendicular to the direction of propagation. In polarized light, the oscillations are restricted to specific directions.

There are three primary types of polarization:

- **Linear Polarization**: The electric field oscillates in a single plane. This can be further classified into horizontal and vertical polarization, depending on the orientation of the oscillation.
- **Circular Polarization**: The electric field vector rotates in a helical pattern as the light propagates. This can be right-handed or left-handed, depending on the rotation direction.
- **Elliptical Polarization**: This is a general form of polarization where the electric field vector describes an ellipse in any given plane perpendicular to the direction of propagation. Linear and circular polarizations are special cases of elliptical polarization.

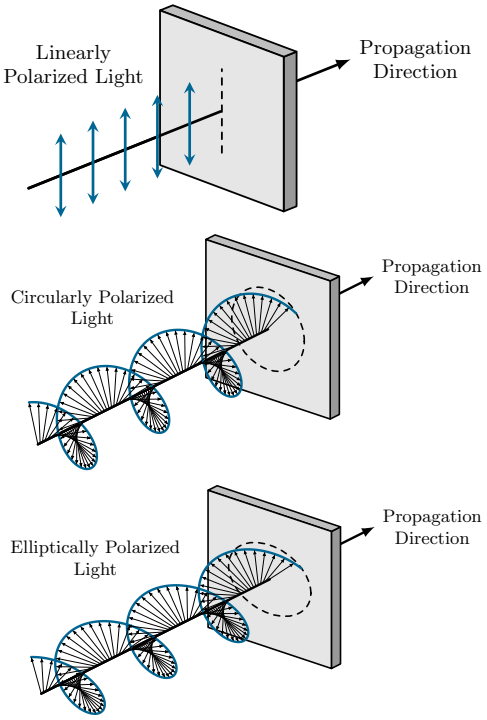


**Figure 2.3:** *Types of polarized light waves*

### 2.2.2 Detection of Polarized Light

In order to recover more information about a scene through light propagation's characteristics, detection techniques need to be implemented.

Most polarization detection techniques involve using a set of polarizing filters in front of a camera. This technique is called Polarimetric Imaging and can reveal surface properties or stress patterns by analyzing the polarization state across the scene.

Polarizing filters are optical elements that selectively transmit light in a specific polarization state. Common types include:

- **Linear Polarizers**: These filters transmit light with electric fields oscillating in a specific direction while blocking perpendicular components. They are used in photography, LCD screens, and scientific instruments.

- **Circular Polarizers**: These consist of a linear polarizer followed by a quarter-wave plate, which converts linearly polarized light into circularly polarized light and vice versa.

In addition to polarizing filters, polarimetry imaging uses the Stokes parameters to obtain the polarization state of light.

### 2.2.3 Polarization in Imaging

Polarization imaging enhances the capabilities of traditional imaging systems by providing additional contrast mechanisms. Applications include:

- **Biomedical Imaging** [15]: Polarization can differentiate between healthy and diseased tissues, detect birefringent structures like collagen, and improve contrast in microscopy.
- **Remote Sensing**: Polarization measurements from satellites and aircraft can detect surface features, atmospheric particles, and water bodies with greater accuracy. The work developed for imaging through scattering media [18] is a good example of polarimetric imaging that can be used for this application.
- **Material Science**: Analyzing the polarization of reflected light can reveal surface roughness, stress distributions, and structural properties of materials [19].

Despite its advantages, polarization imaging faces several challenges [10]:

- **Alignment and Calibration**: Precise alignment of polarizing elements and accurate calibration are crucial for reliable measurements.
- **Environmental Influences**: Ambient light, reflections, and scattering can affect polarization measurements, necessitating careful control and correction.
- **Data Processing**: Interpreting polarization data requires complex algorithms and can be computationally intensive, especially for real-time applications.

## 2.3 Methodology followed

The purpose of this Master's thesis is to develop a system that can detect linearly polarized light and determine its orientation in a single image using lensless imaging. This was achieved in the conception of a lensless polarization camera that uses very specific materials to obtain a full-Stokes imaging system [6]. However, we aim to develop a system that is accessible and easily reproduced. This is realized by integrating a set of linear polarizers into the DiffuserCam setup, the innovative imaging system developed by Laura Waller's team [3]. The following subsections outline the key components and steps involved in this methodology.

### 2.3.1 DiffuserCam System

The DiffuserCam is an optical system that captures the light information of a scene using a diffuser and a conventional camera sensor. The diffuser used is tape, where

the glue scatters incoming light in a known, random pattern. The camera sensor then captures this scattered light, and computational algorithms are used to reconstruct the image. This system allows for lensless imaging and has the advantage of being compact and cost-effective. The DiffuserCam's implementation is reproduced in Chapter 3 of this work.

### 2.3.2 Integration of Linear Polarizers

To enable the detection of linearly polarized light, a set of linear polarizers is placed between the diffuser and the camera sensor. The polarizers are oriented at different angles, specifically at 0°, 45°, 90°, and 135°. This configuration allows the system to capture the intensity of light transmitted through each polarizer orientation in a single shot. The mathematical model and final produced setup of the so-called PolariCam are developed in Chapter 4.

In the experimental setup, light from the scene passes through the diffuser, which scatters the light. This scattered light then passes through the set of linear polarizers before reaching the camera sensor. The camera captures the intensity patterns corresponding to each polarizer orientation simultaneously.

The captured data consists of four intensity images, each corresponding to one of the polarizer orientations (0°, 45°, 90°, and 135°). These intensity images are denoted as $I_0$, $I_{45}$, $I_{90}$, and $I_{135}$ respectively.

### 2.3.3 Polarization State Determination

To determine the polarization state of the light, the captured intensity data is processed to compute the phase shift between the vector of the light source's components as well as the Stokes parameters. These Stokes parameters provide a complete description of the polarization state of the light, including its intensity ($I$), degree of linear polarization along different axes ($Q$ and $U$).

### 2.3.4 Validation and Calibration

Validation and calibration procedures ensure the system's accuracy and reliability. Using known polarized light sources, the system's response is tested, and systematic errors are adjusted. Calibration corrects discrepancies caused by the diffuser, polarizers, or camera sensor. The system's performance is evaluated by comparing reconstructed images with theoretical predictions and ground truth measurements, using metrics like accuracy, precision, and robustness.

### 2.3.5 Sources of Errors

The accurate detection of linearly polarized light can be influenced by several sources of error. These errors can arise from the light source, optical elements, the environment, and the computational processes involved in image reconstruction. Understanding these error sources is crucial for improving the precision and reliability of polarization measurements.

#### External Noise

Physical noise sources, such as dust particles on optical components or the sensor, can scatter light and introduce artifacts into the measurements. Thermal noise, caused by the random motion of electrons in the sensor, can also degrade image quality. Thermal noise increases with temperature, making it important to maintain stable and controlled environmental conditions during measurements.

#### Saturation of the sensor

Saturation errors in camera sensors occur when light intensity exceeds the sensor's dynamic range, causing pixels to reach their maximum value. The result is a clipping of highlights and a loss of detail. Saturated pixels can't distinguish brightness levels beyond their capacity, resulting in flat, white areas in images with high contrast. As the PolariCam system is based on definite intensity measurements, sensor saturation is an issue that needs to be addressed beforehand to avoid false results.

#### Filter Attenuation of Intensity

Polarizing filters, while essential for detecting polarized light, inherently attenuate the intensity of the transmitted light. This attenuation reduces the signal-to-noise ratio (SNR) and can affect the accuracy of the polarization measurements, especially in low-light conditions. To assess this type of issue, the calibration step of the polarization detection includes measurements to obtain the transmission ratio between the captured intensity of the light going through polarizers and the original measurements without a filter. This is done in Chapter 4.

# 3

# DiffuserCam

The DiffuserCam [3] developed by Laura Waller and her team is implemented and explained in this chapter. This concept of a lensless camera is used to create a compact and low cost end device.

The DiffuserCam algorithm reconstructs images from the light scattered by a diffuser forming a caustic pattern on the sensor. The main steps include calibration, forward modeling and inverse problem solving using optimization techniques.

## 3.1 Construction and Calibration

The physical design of the DiffuserCam involves using a small lensless camera and placing tape in front of it to act as a diffuser. In this work, a PiCamera (Figure 3.1a) whose lens must be removed before the experiments and a double-sided tape (Figure 3.1b) were used, as explained in the building guide [9]. The physical installation is shown in Figure 3.2.

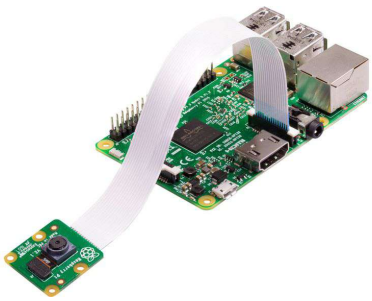

**(a)** *RaspberryPi and PiCamera [22]*

**(b)** *Double-sided tape [2]*

**Figure 3.1:** *Principal materials used for the construction of the DiffuserCam*


**Figure 3.2:** *Physical installation of the DiffuserCam*

### 3.1.1 Evaluation of the PSFs

Key variables in the setup include the distance between the sensor and the diffuser, the focal distance $d_f$, and the distance between the diffuser and the point light source, referred to as $d_s$. Evaluating these distances, represented in Figure 3.3, during the installation is crucial for focusing the camera and obtaining meaningful results. This involves observing the caustic pattern resulting from the Point Spread Function (PSF) of the diffuser, as shown in Figure 3.4.

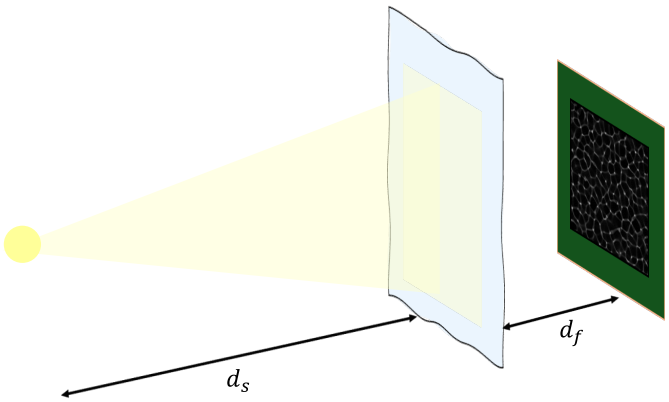


**Figure 3.3:** *Distances variables $d_s$ and $d_f$*

When the diffuser is properly focused, the caustic lines should be thin with high contrast, spanning multiple directions. The quantitative metric for comparing PSFs and evaluating the optimal one is the Full Width at Half Maximum (FWHM) of the PSF's auto-correlation peak [13]. Achieving minimal width indicates the optimal PSF, resulting in appropriate focal distance, $d_f$, and source distance, $d_s$.

First, by moving the camera sensor closer to the diffuser at each measurement, one can observe the influence of the focal distance on the PSF's auto-correlation. The results are shown in Figure 3.5 for a fixed source distance $d_s = 50cm$.

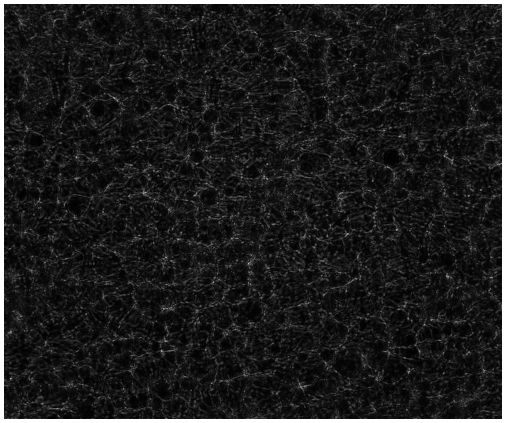

**Figure 3.4:** *Caustic pattern resulting from the Point Spread Function (PSF) of the diffuser*

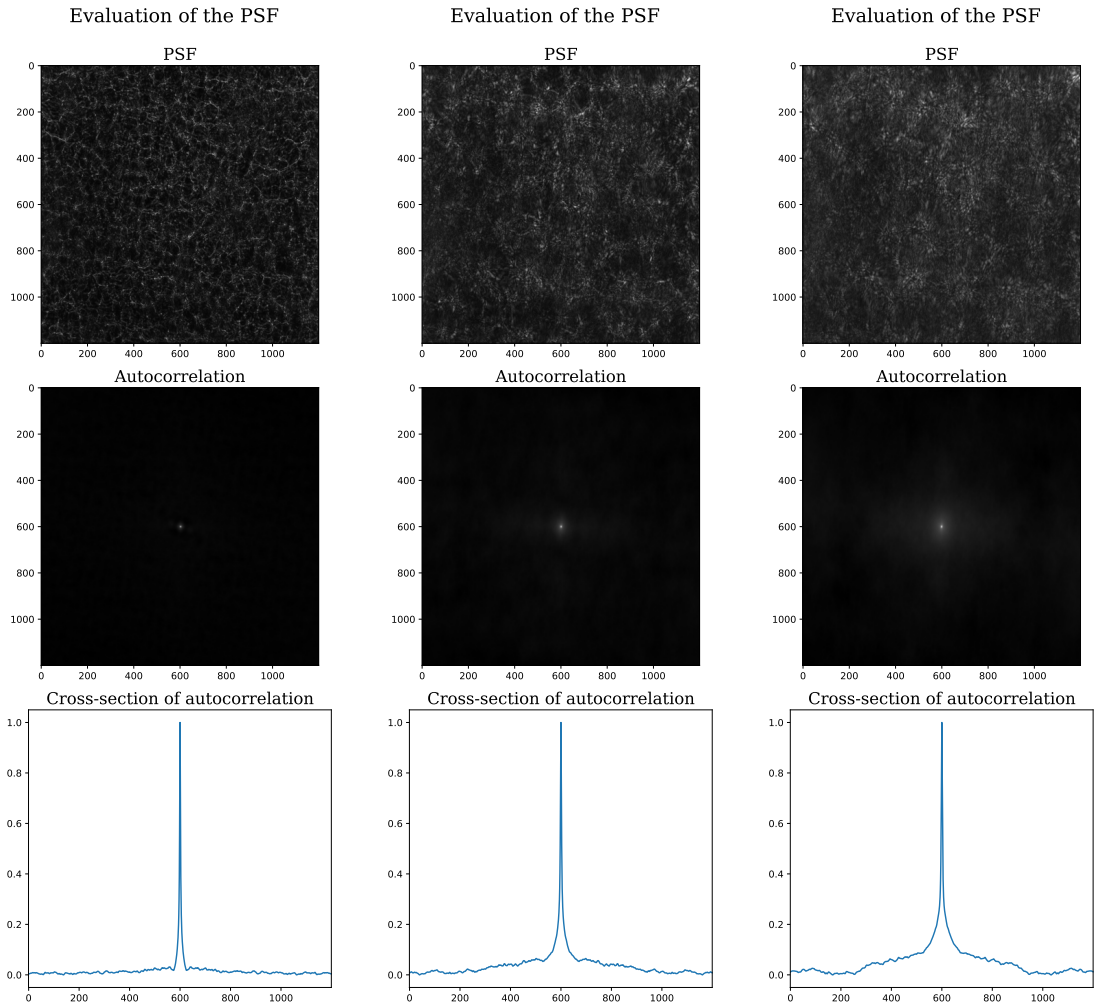


**(a)** *Auto-correlation results for* $d_f = 0.1cm$

**(b)** *Auto-correlation results for* $d_f = 0.5cm$

**(c)** *Auto-correlation results for* $d_f = 0.9cm$

**Figure 3.5:** *Auto-correlation results for a PSF evaluated at different focal distances,* $d_f$ *and* $d_s = 50cm$

The evaluation of the FWHM corresponding to the cross-section of each auto-correlation

in Figure 3.5 is given in Table 3.1.

| | $\mathbf{d_f = 0.1cm}$ | $\mathbf{d_f = 0.5cm}$ | $\mathbf{d_f = 0.9cm}$ |
|---|---|---|---|
| **Peak FWHM** $[pxl/1200]$ | 4.618 | 6.235 | 6.779 |

**Table 3.1:** *Evaluation of the auto-correlation curves for the PSF calibration with different focal distances, $d_f$, and $d_s = 50cm$*

The results show that the minimal width is obtained for a minimal focal distance $d_f = 0.1cm$.

Then, for a fixed focal distance $d_f = 0.3cm$, the variation of the source distance $d_s$ gives the results depicted in Figure 3.6.

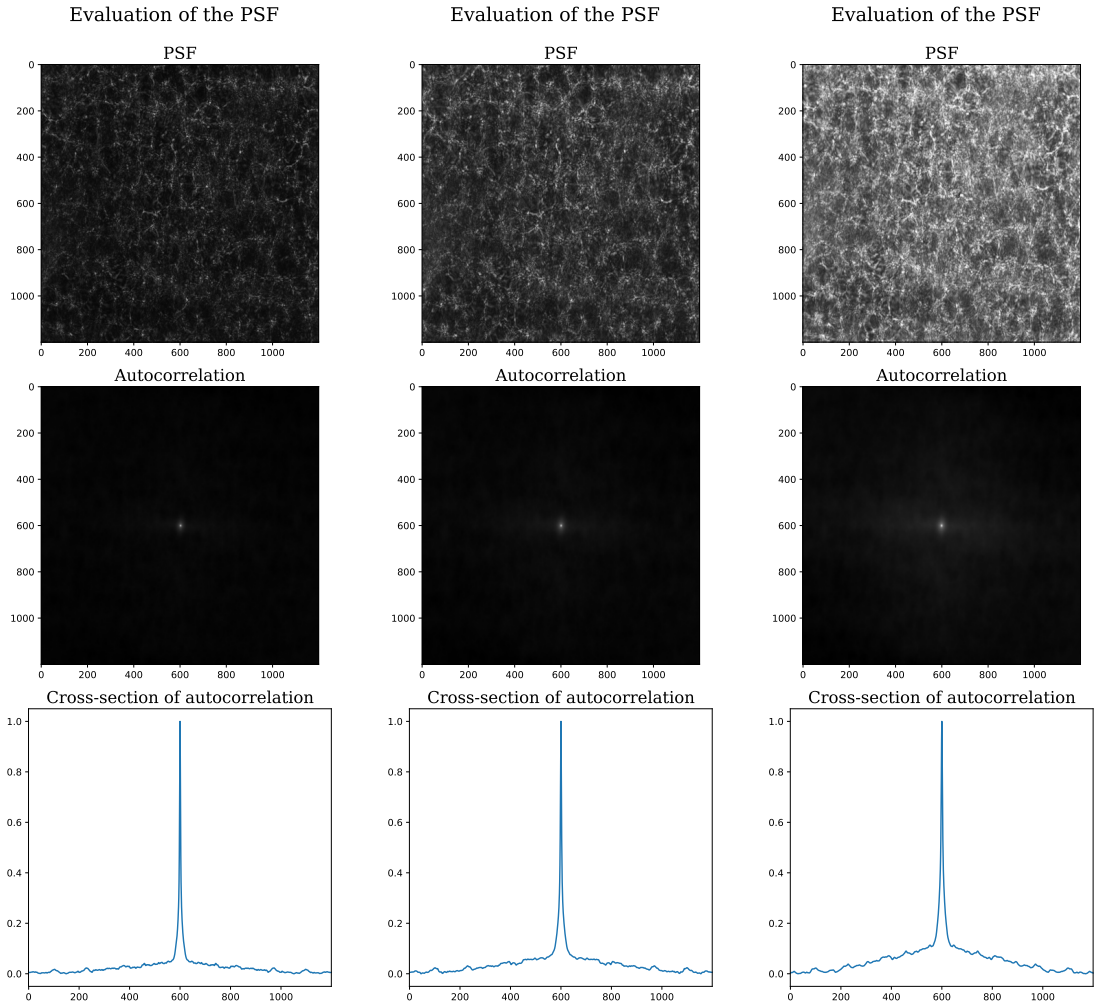


**(a)** *Auto-correlation results for $d_s = 50cm$*

**(b)** *Auto-correlation results for $d_s = 35cm$*

**(c)** *Auto-correlation results for $d_s = 20cm$*

**Figure 3.6:** *Auto-correlation results for a PSF evaluated at different source distances*

The FWHM corresponding to the cross-section of each auto-correlation in Figure 3.6 are computed and gathered in Table 3.2. The farther away the source is, the better the results are.

| | $\mathbf{d_s}$ **= 20cm** | $\mathbf{d_s}$ **= 35cm** | $\mathbf{d_s}$ **= 50cm** |
|---|---|---|---|
| **Peak FWHM** $[pxl/1200]$ | 8.872 | 6.667 | 5.599 |

**Table 3.2:** *Evaluation of the auto-correlation curves for the PSF calibration with different source-diffuser distances, $d_s$, and $d_f = 0.3cm$*

The evolution of the Full Width at Half Maximum with respect to the focal distance and for various source distances is rendered in a graph in Figure 3.7.

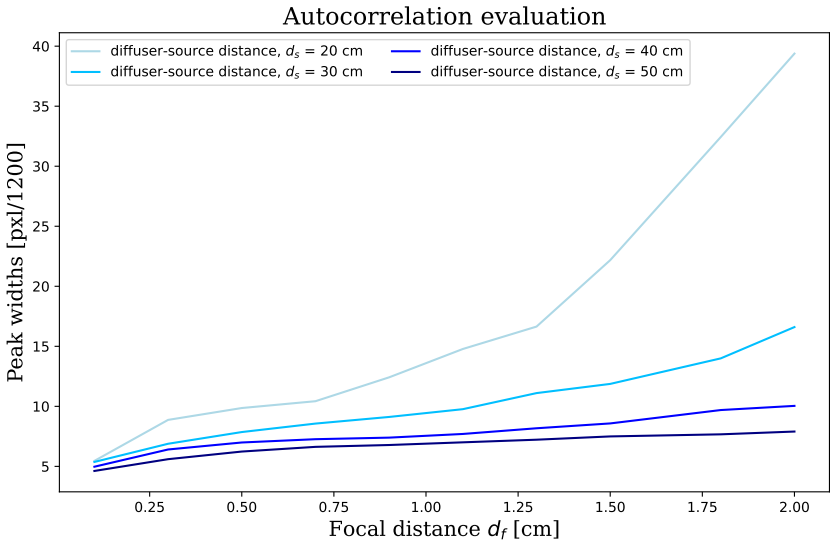


**Figure 3.7:** *Evolution of the auto-correlation's cross-section with respect to the focal distance, for different source distances*

The measurements suggest that positioning the light source farther from the diffuser while bringing the sensor closer to the diffuser yields the most favorable Point Spread Function (PSF). However, the camera being calibrated with a source far from the sensor will result in a smaller image at reconstruction. This observation is shown later in the chapter, in Section 3.3.

### 3.1.2 Hypothesis of the DiffuserCam

The final imaging system is based on the assumptions of linearity and shift-invariance, thereby enabling the forward model described subsequently in Section 3.2. To observe these assumptions, we need to create an aperture in front of the camera setup.

The dimensions of the sensor are specified in the Raspberry camera module documentation [12] as $3.68 \times 2.76\ mm$. To take account of the aperture required, this area is then reduced using opaque black adhesive tape. The modeling and result of this aperture are represented in Figure 3.8.

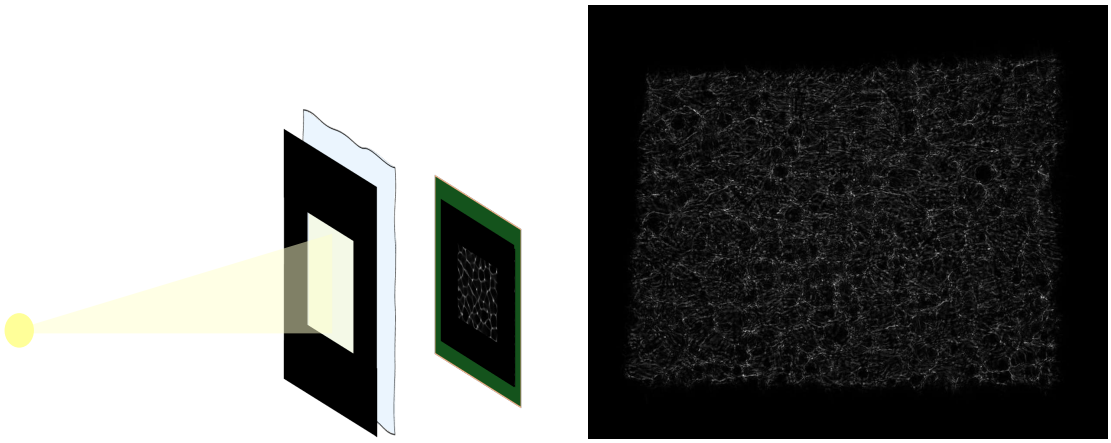

**(a)** *Modeling of the PSF captured with an aperture* **(b)** *Impact of the aperture on the PSF*

**Figure 3.8:** *Aperture in front of the diffuser and the camera sensor*

The system is therefore shift-invariant, meaning that the sensor reading of the PSF shifts along with the shift of the source, as depicted in Figure 3.9.

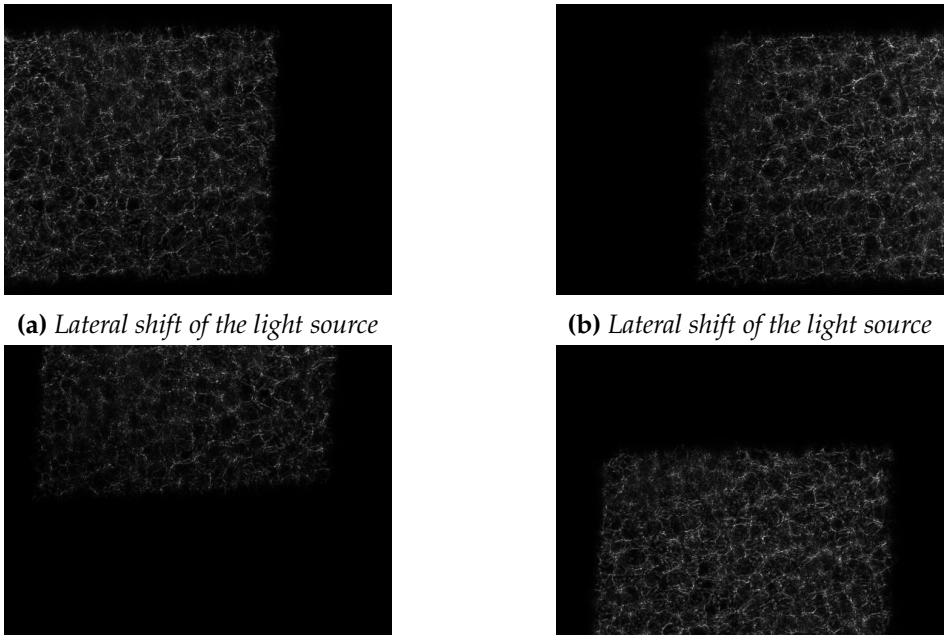

**(a)** *Lateral shift of the light source* **(b)** *Lateral shift of the light source*

**(c)** *Vertical shift of the light source* **(d)** *Vertical shift of the light source*

**Figure 3.9:** *Impact of the light source shifting on the PSF*

Moreover, we consider that the sensor has a linear response to light intensity. This results in a direct correlation between adjustments made to the intensity of a point

source and changes in the sensor readings.

Finally, given the inconsistency of the light sources, the Point Spread Function (PSF) resulting from two distinct sources is the superposition of their individual PSF. This can be observed in Figure 3.10. Consequently, the assumption of linearity is supported.

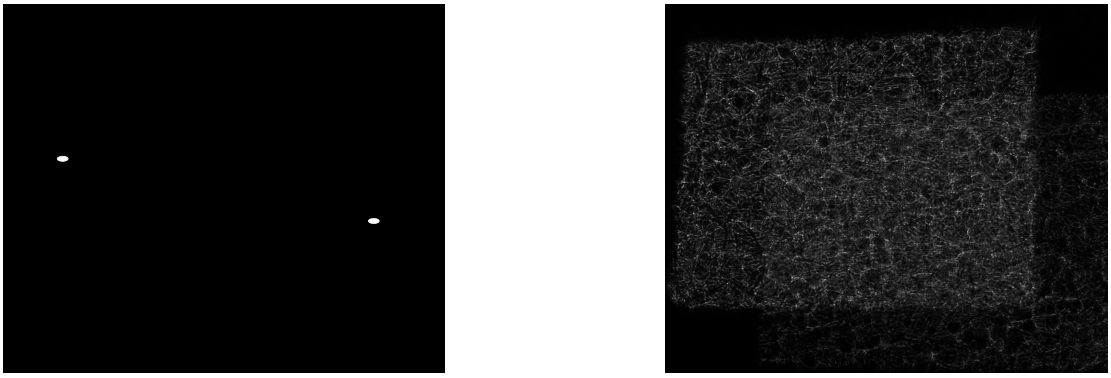

**Figure 3.10:** *Contributions of two point sources resulting in their superposition.*

## 3.2 Image Reconstruction

In order to reconstruct the image captured by the DiffuserCam, as opposed to a traditional lens camera, the data must be processed using an algorithm to solve an optimization problem. The first step is to specify the forward model of the camera, then formulate the inverse problem and apply specific algorithms for solving the problem [8]. These steps are described in this section.

### 3.2.1 Forward Model

The core problem in image reconstruction for DiffuserCam is to model the light propagation from the object scene to the sensor. The signal captured by the DiffuserCam is denoted $b$ while the image needed to be reconstructed is $v$.

As shown in Subsection 3.1.2, the system is linear and shift-invariant (LSI). The light intensity distribution $v$ at the scene can be represented as a sum of point sources. The captured signal $f(v)$ is represented by a 2D convolution between the light source signal $v$ and Point Spread Function $h$ such as in equation 3.1.

$$b = f(v) = h * v \tag{3.1}$$

In practice, $f$ is treated as a matrix operation. Since matrices operate on vectors, the images are vectorized by stacking the columns. For an $m \times n$ sensor, the image becomes a vector of length $mn$. Thus, the convolution can be represented as:

$$f(v) = h * v \iff f(\mathbf{v}) = \mathbf{M}\mathbf{v} \tag{3.2}$$

However, the sensor captures only part of this convolution due to its finite size. Hence, the sensor reading is a cropped convolution: The forward model can be expressed with

$$f(v) = \text{crop}(h * v) \iff f(\mathbf{v}) = \mathbf{C}\mathbf{M}\mathbf{v} = \mathbf{A}\mathbf{v} \tag{3.3}$$

where $\mathbf{C}$ represents the cropping operation and $\mathbf{A}$ is shorthand for $\mathbf{CM}$.

### 3.2.2 Inverse Problem

To reconstruct $v$ from $b$, the problem $Av = b$ needs to be solved. Direct inversion of $A$ is not possible due to loss of information in the cropping operation, making $\mathbf{C}$ non-invertible, while the convolution with $h$ may also not be invertible, making $\mathbf{M}$ potentially non-invertible.
Thus, the reconstruction is framed as an optimization problem:

$$\mathbf{v}^* = \arg\min_{\mathbf{v}} \frac{1}{2}\|\mathbf{A}\mathbf{v} - \mathbf{b}\|_2^2 \tag{3.4}$$

Given that $\mathbf{A}$ is large (on the order of $10^{12}$ entries for a typical sensor), storing it in memory is impractical. Therefore, algorithms using the linear operators of $f$, specifically crop and convolution, which have efficient 2D implementations, are required.

### 3.2.3 Algorithms

To solve for $\mathbf{v}$, the main methods developed in Laura Waller's work [8] are the Gradient Descent (GD) and the Alternating Direction Method of Multipliers (ADMM). These algorithms are quickly described here under with the main mathematical expressions implemented.

#### Gradient Descent (GD)

Gradient descent iteratively minimizes a convex function by moving in the direction of the negative gradient. For this problem:

$$g(\mathbf{v}) = \frac{1}{2}\|\mathbf{A}\mathbf{v} - \mathbf{b}\|_2^2 \tag{3.5}$$

$$\nabla_{\mathbf{v}} g(\mathbf{v}) = \mathbf{A}^H(\mathbf{A}\mathbf{v} - \mathbf{b}) \tag{3.6}$$

Here, $\mathbf{A}^H$ is the adjoint of $\mathbf{A}$. Using properties of linear operators:

$$\mathbf{A}\mathbf{v} = \mathbf{C}\mathbf{M}\mathbf{v} \quad \Rightarrow \quad \mathbf{A}^H\mathbf{v} = \mathbf{M}^H\mathbf{C}^H\mathbf{v} \tag{3.7}$$

The adjoint of the convolution $M$ is represented using Fourier transforms. The Fourier

operator $\mathcal{F}$ and its properties along with the convolution theorem are expressed in the following expressions, from Equation 3.8 to Equation 3.10.

$$h * v = \mathcal{F}^{-1}\left(\mathcal{F}(h) \cdot \mathcal{F}(v)\right) \tag{3.8}$$

$$\mathcal{F}(v) \Longleftrightarrow \mathbf{Fv} \tag{3.9}$$

$$\mathcal{F}(h) \cdot \mathcal{F}(v) \Longleftrightarrow \text{diag}(\mathbf{Fh})\mathbf{Fv} \tag{3.10}$$

This results in Expression 3.12.

$$\mathbf{Mv} \Longleftrightarrow \mathbf{F}^{-1}(\text{diag}(\mathbf{Fh})\mathbf{Fv}) \tag{3.11}$$

$$\mathbf{M}^H\mathbf{v} = \mathbf{F}^{-1}(\text{diag}(\mathbf{Fh})^*\mathbf{Fv}) \tag{3.12}$$

The adjoint of the cropping operation $\mathbf{C}$ is zero-padding. Thus:

$$\mathbf{A} = \mathbf{C}\mathbf{F}^{-1}\text{diag}(\mathbf{Fh})\mathbf{F} \tag{3.13}$$

$$\mathbf{A}^H = \mathbf{F}^{-1}\text{diag}(\mathbf{Fh})^*\mathbf{F}\mathbf{C}^H \tag{3.14}$$

In practical implementation, an initial guess $v_0$ is used, and it is iteratively updated:

$$\mathbf{v}_{k+1} \leftarrow \mathbf{v}_k - \alpha_k \mathbf{A}^H(\mathbf{A}\mathbf{v}_k - \mathbf{b})$$

with $\alpha_k$ as the step size. For efficient computation, Fourier transforms and pointwise multiplications are used, avoiding direct manipulation of $\mathbf{A}$.

It is important to choose the right step size $\alpha$ to ensure that the algorithm converges appropriately. If $\alpha$ is too large, the algorithm may overshoot the minimum and fail to converge. On the other hand, if $\alpha$ is too small, the algorithm will converge very slowly [14].

A key rule concerns the Lipschitz constant $L$ of the gradient of the function $f(v)$. The gradient $\nabla f(v)$ is said to be Lipschitz continuous if there exists a constant $L > 0$ such that for all $v$ and $w$:

$$\|\nabla f(v) - \nabla f(w)\| \leq L\|v - w\|$$

For GD to converge, $\alpha$ must be chosen such that

$$\alpha < \frac{1}{L}$$

This ensures that each step of the gradient descent avoids overshooting the minimum of the function $f(v)$.

**Accelerated Gradient Descent - Nesterov Momentum:** To speed up convergence, a momentum term is added, incorporating the old descent direction into the new one:

$$\begin{aligned}
&\mathbf{v}_0 = \frac{I}{2},\ \mu = 0.9,\ \mathbf{p}_0 = 0 \\
&\text{for } k \in [0, iters]: \\
&\quad \mathbf{p}_{k+1} \leftarrow \mu \mathbf{p}_k - \alpha_k \nabla g(\mathbf{v}_k) \\
&\quad \mathbf{v}'_{k+1} \leftarrow \mathbf{v}_k - \mu \mathbf{p}_k + (1+\mu)\mathbf{p}_{k+1} \\
&\quad \mathbf{v}_{k+1} \leftarrow \text{proj}_{\mathbf{v}\geq 0}(\mathbf{v}'_{k+1})
\end{aligned}$$

**Fast Iterative Shrinkage-Thresholding Algorithm (FISTA):** This algorithm further accelerates the descent by incorporating a proximal step.

$$\begin{aligned}
&\mathbf{v}_0 = \frac{I}{2},\ t_1 = 1,\ x_0 = \mathbf{v}_0 \\
&\text{for } k \in [0, iters]: \\
&\quad x_k \leftarrow p_L(v_k) \\
&\quad t_{k+1} \leftarrow \frac{1 + \sqrt{1 + 4t_k^2}}{2} \\
&\quad \mathbf{v}_{k+1} \leftarrow x_k + \frac{t_k - 1}{t_{k+1}}(x_k - x_{k-1})
\end{aligned}$$

**Alternating Direction Method of Multipliers (ADMM)**

ADMM is particularly effective for problems involving separable objectives or constraints [11]. The optimization problem is rewritten to introduce auxiliary variables in Equation 3.15.

$$\mathbf{v} = \arg\min_{w\geq 0, u, x} \frac{1}{2}\|\mathbf{b} - \mathbf{C}x\|_2^2 + \tau\|u\|_1 \tag{3.15}$$

Such that $x = \mathbf{M}\mathbf{v}$, $w = \mathbf{v}$, $u = \Psi\mathbf{v}$.

The augmented Lagrangian for this problem is:

$$\begin{aligned}
\mathcal{L}(\{\mathbf{v}, x, w, u\}, \{\xi, \eta, \rho\}) = &\frac{1}{2}\|\mathbf{b} - \mathbf{C}x\|_2^2 + \tau\|u\|_1 + I_+(w) \\
&+ \frac{\mu_1}{2}\|\mathbf{M}\mathbf{v} - x\|_2^2 + \xi^T(\mathbf{M}\mathbf{v} - x) \\
&+ \frac{\mu_2}{2}\|\Psi\mathbf{v} - u\|_2^2 + \eta^T(\Psi\mathbf{v} - u) \\
&+ \frac{\mu_3}{2}\|\mathbf{v} - w\|_2^2 + \rho^T(\mathbf{v} - w)
\end{aligned}$$

Here, $\xi$, $\eta$, and $\rho$ are the dual variables (Lagrange multipliers), and $\mu_1$, $\mu_2$, and $\mu_3$ are

penalty parameters.

The ADMM algorithm alternates between updating the variables $x$, $w$, $u$, $\mathbf{v}$, and the dual variables $\xi$, $\eta$, and $\rho$. The steps are as follows for $k \in [0, iters]$.

1. **Update $u$:**

$$u_{k+1} \leftarrow \text{SoftThresh}(\Psi \mathbf{v}_k + \frac{\eta_k}{\mu_2}, \frac{\tau}{\mu_2}) \tag{3.16}$$

   with the soft-thresholding operator used defined as:

$$\text{SoftThresh}(x, \tau) = \text{sign}(x) \max(|x| - \tau, 0) \tag{3.17}$$

2. **Update $x$:**

$$x_{k+1} \leftarrow (\mathbf{C}^T\mathbf{C} + \mu_1 I)^{-1}(\mathbf{C}^T\mathbf{b} + \mu_1 \mathbf{M}\mathbf{v}_k + \xi_k) \tag{3.18}$$

3. **Update $w$:**

$$w_{k+1} \leftarrow \max\left(\frac{\rho_k}{\mu_3} + \mathbf{v}_k, 0\right) \tag{3.19}$$

4. **Update v:**

$$\mathbf{v}_{k+1} \leftarrow (\Psi^T\Psi + \mu_1 \mathbf{M}^T\mathbf{M} + \mu_3 I)^{-1} r_k \tag{3.20}$$

   where

$$r_k = \mu_3 w_{k+1} - \rho_k + \Psi^T(\mu_2 u_{k+1} - \eta_k) + \mathbf{M}^T(\mu_1 x_{k+1} - \xi_k)$$

5. **Update dual variables $\xi, \eta, \rho$:**

$$\xi_{k+1} \leftarrow \xi_k + \mu_1(x_{k+1} - \mathbf{M}\mathbf{v}_{k+1})$$

$$\eta_{k+1} \leftarrow \eta_k + \mu_2(u_{k+1} - \Psi\mathbf{v}_{k+1})$$

$$\rho_{k+1} \leftarrow \rho_k + \mu_3(w_{k+1} - \mathbf{v}_{k+1})$$

## 3.3 DiffuserCam Image Reconstruction Results

Once the setup has been installed and the reconstruction algorithms have been implemented, images can be reconstructed using the DiffuserCam. Using simple black and white source images such as the ones illustrated in Figure 3.11, the parameters of the DiffuserCam reconstruction processes are analyzed in this section. The two parameters considered are the downsampling factor $f = \frac{1}{2^k}$ with $k$ a positive integer, and the number of iterations in the process $iters$. These parameters need to be set in the configuration file associated with the chosen reconstruction algorithm.

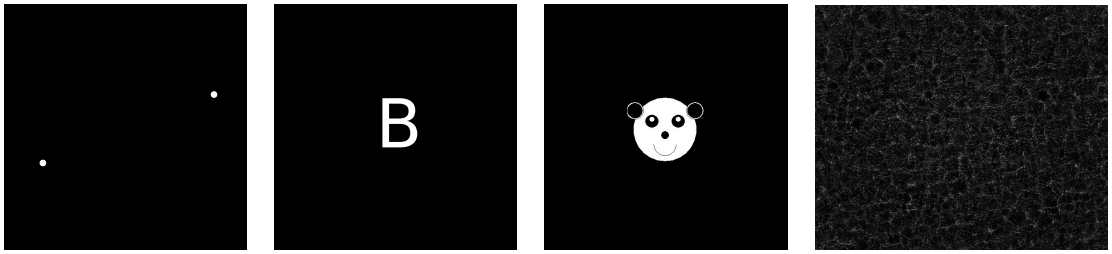

**(a)** *Original image of 2 punctual sources* **(b)** *Original image of the letter B* **(c)** *Original image of a simple panda drawing* **(d)** *Captured PSF used for the reconstruction*

**Figure 3.11:** *Original images used for the reconstruction algorithm tests and the captured PSF*

### 3.3.1 Simulation results

In order to better observe the influence of the reconstruction algorithm parameters on the final image reconstruction, the raw data were simulated to avoid environmental noise due to poor scene lighting or other physical factors. The raw data were simulated by convolution between the original images and the captured PSF. The raw data obtained by simulation are shown in Figure 3.12.

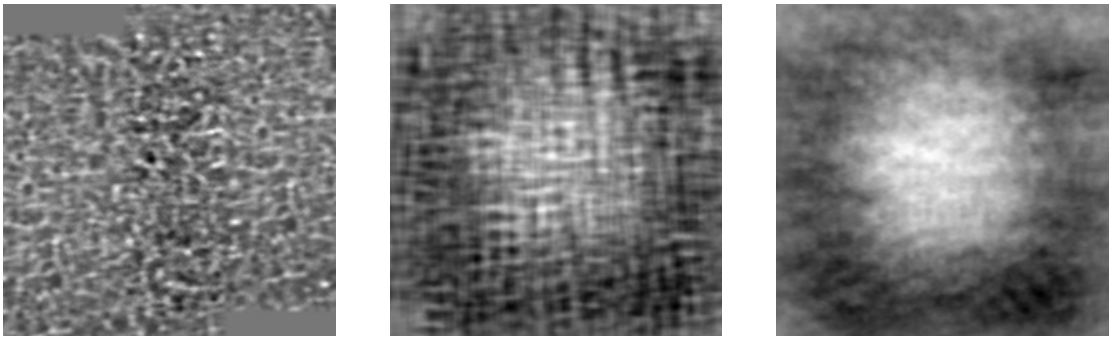

**(a)** *Simulated raw data of 2 punctual sources* **(b)** *Simulated raw data of the letter B* **(c)** *Simulated raw data of a simple panda drawing*

**Figure 3.12:** *Simulated raw data*

Four different configurations were implemented into the image reconstruction algorithms for each parameter to evaluate. They are provided in Tables 3.3 and 3.4.

| Evaluated parameter | Config. 1 | Config. 2 | Config. 3 | Config. 4 | Fixed parameter |
|---|---|---|---|---|---|
| **Downsampling factor,** $f$ | 0.0625 | 0.125 | 0.25 | 0.5 | $iters = 150$ |
| **Number of iterations,** $iters$ | 10 | 75 | 200 | 500 | $f = 0.25$ |

**Table 3.3:** *GD configuration parameters*

The downsampling factor $f$ corresponds to the reduction in resolution of the image the algorithm is going to be applied to. Therefore, as it can be seen in the reconstruction results for various $f$ values in Figures 3.13 and 3.14, the smaller the resolution is, the

| Evaluated parameter | Config. 1 | Config. 2 | Config. 3 | Config. 4 | Fixed parameter |
|---|---|---|---|---|---|
| **Downsampling factor,** $f$ | 0.0625 | 0.125 | 0.25 | 0.5 | $iters = 15$ |
| **Number of iterations,** $iters$ | 3 | 10 | 30 | 50 | $f = 0.25$ |

**Table 3.4:** *ADMM configuration parameters*

less accurate the reconstructions appear compared to the original images.

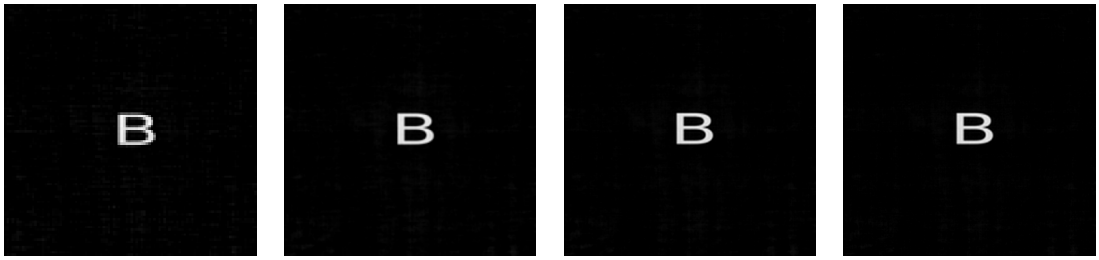

**(a)** $f = 0.0625$ **(b)** $f = 0.125$ **(c)** $f = 0.25$ **(d)** $f = 0.5$

**Figure 3.13:** *Gradient Descent reconstruction with simulated raw data for different downsampling factors*

**(a)** $f = 0.0625$ **(b)** $f = 0.125$ **(c)** $f = 0.25$ **(d)** $f = 0.5$

**Figure 3.14:** *Alternating Direction Method of Multipliers reconstruction with simulated raw data for different downsampling factors*

The influence of the number of iterations on the image reconstructions can be observed in Figures 3.15 and 3.16. Qualitatively, as the number of iterations increases, both GD and ADMM reconstructions give more detailed and precise results compared to the original images.

### 3.3.2 Image Reconstruction Quality Metrics

To evaluate quantitatively the reconstructions, the following metrics are used and can therefore assess the quality of the reconstructed images [7].

- **The Mean Squared Error (MSE)**: measures the average squared difference between the original and reconstructed image pixels. The smaller the error is, the better

**(a)** *Number of iterations = 10* **(b)** *Number of iterations = 75* **(c)** *Number of iterations = 200* **(d)** *Number of iterations = 500*

**Figure 3.15:** *Gradient Descent reconstruction with simulated raw data for different number of iterations*

**(a)** *Number of iterations = 3* **(b)** *Number of iterations = 10* **(c)** *Number of iterations = 30* **(d)** *Number of iterations = 50*

**Figure 3.16:** *Alternating Direction Method of Multipliers reconstruction with simulated raw data for different number of iterations*

the image reconstruction is. If $I$ and $K$ are two images of dimensions $M \times N$, the MSE is defined as:

$$\text{MSE} = \frac{1}{MN} \sum_{i=1}^{M} \sum_{j=1}^{N} (I(i,j) - K(i,j))^2 \tag{3.21}$$

- **Peak Signal-to-Noise Ratio (PSNR)**: quantifies the ratio between the maximum possible power of a signal and the power of corrupting noise. The higher the ratio, the more accurate the reconstruction is. It is given by:

$$\text{PSNR} = 10 \cdot \log_{10} \left( \frac{L^2}{\text{MSE}} \right) \tag{3.22}$$

  where $L$ is the maximum possible pixel value of the image.

- **The Structural Similarity Index (SSIM)**: assesses the similarity between two images based on luminance, contrast, and structure. A higher value results in a higher similarity level. It is defined as:

$$\text{SSIM}(x,y) = \frac{(2\mu_x\mu_y + C_1)(2\sigma_{xy} + C_2)}{(\mu_x^2 + \mu_y^2 + C_1)(\sigma_x^2 + \sigma_y^2 + C_2)} \tag{3.23}$$

where:

$$\mu_x = \text{average of } x \qquad \sigma_{xy} = \text{covariance of } x \text{ and } y$$
$$\mu_y = \text{average of } y \qquad C_1 = (K_1 L)^2$$
$$\sigma_x^2 = \text{variance of } x \qquad C_2 = (K_2 L)^2$$
$$\sigma_y^2 = \text{variance of } y$$

$C_1$ and $C_2$ are constant terms used to avoid zero-divisions, with $K_1$ and $K_2$, some small constants.

- **The Learned Perceptual Image Patch Similarity (LPIPS)**: is a metric designed to assess the perceptual similarity between two images using deep neural network features. A smaller value leads to a higher similarity level.

  If $F(x)$ and $F(y)$ represent the feature maps of images $x$ and $y$ obtained from a neural network, LPIPS is defined as:

$$\text{LPIPS}(x, y) = \sum_l \frac{1}{H_l W_l} \sum_{h=1}^{H_l} \sum_{w=1}^{W_l} \|F_l(x)_{hw} - F_l(y)_{hw}\|_2^2 \tag{3.24}$$

  where:

$$F_l(x) = \text{feature map of image } x \text{ at layer } l$$
$$F_l(y) = \text{feature map of image } y \text{ at layer } l$$
$$H_l = \text{height of the feature map at layer } l$$
$$W_l = \text{width of the feature map at layer } l$$
$$\|\cdot\|_2 = \text{Euclidean distance (or } L2 \text{ norm)}$$

### 3.3.3 Evaluation and discussion

First, the reconstructed images for the letter B are being evaluated using the previously developed metrics to assess the quality of the reconstruction. The results are given in the graphs in Figure 3.17 and Figure 3.18.

The evolution of the metrics with respect to the downsampling factor and the number of iterations leads to the same conclusion as in the qualitative observations of the reconstructions. The results are more accurate for a larger number of iterations and a higher value of the downsampling factor.

Moreover, the Gradient Descent algorithm can be compared to the Alternating Direction Method of Multipliers using the graphs from Figure 3.18. They show that for the same number of iterations and factor of downsampling ($iter = 10$ and $f = 0.25$), the ADMM reconstruction gives better results. In order to obtain the same metric values, the GD

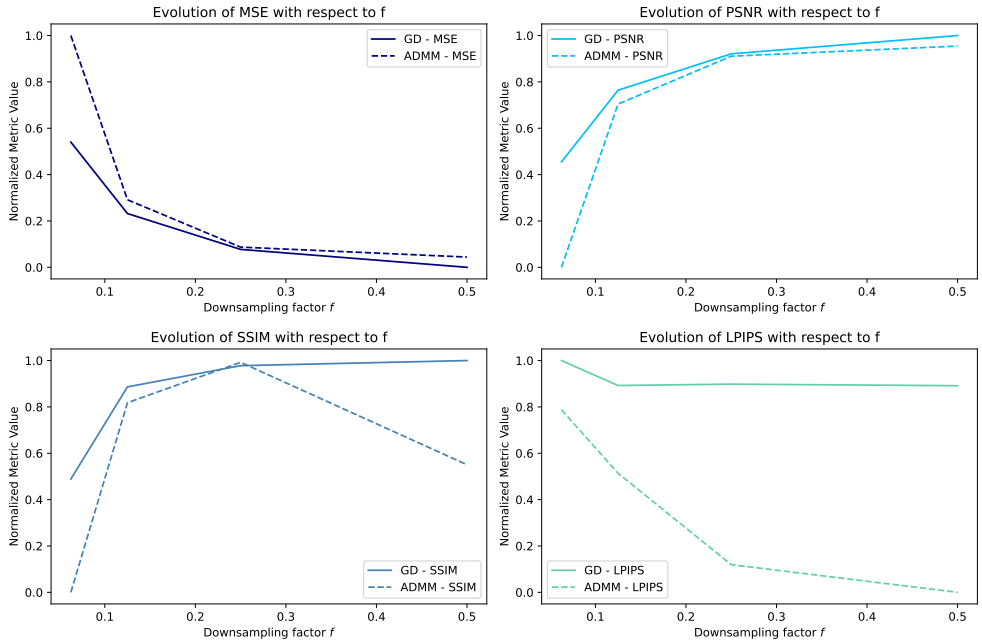


**Figure 3.17:** *Graphs of the metrics with respect to the downsampling factor* $f$

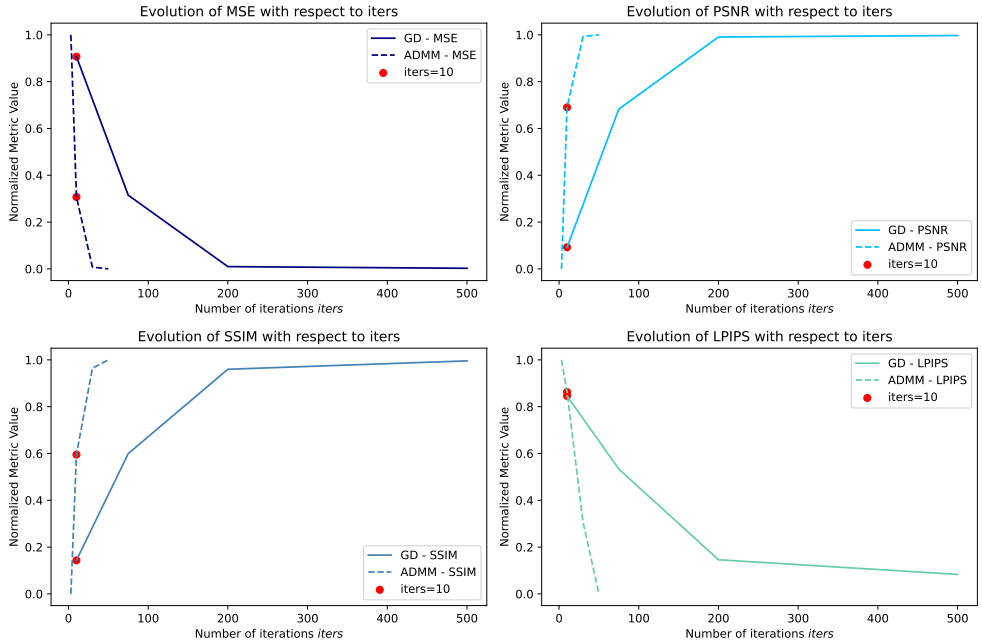


**Figure 3.18:** *Graph of the metrics with respect to the number of iterations* `iters`

algorithm will need a larger amount of iterations, resulting in higher computational times.

To evaluate the quality of image reconstruction for diverse sources in terms of complexity, such as details and shape, the algorithms are applied to the three different original images from Figure 3.11 for each configuration that is considered.

The simulation results obtained for each original image with both reconstruction methods are shown in Figure 3.19 for the GD algorithm and in Figure 3.20 for the ADMM algorithm. These results were recovered using the configuration file with the highest downsampling factor (Config. 4: $f = 0.5$).

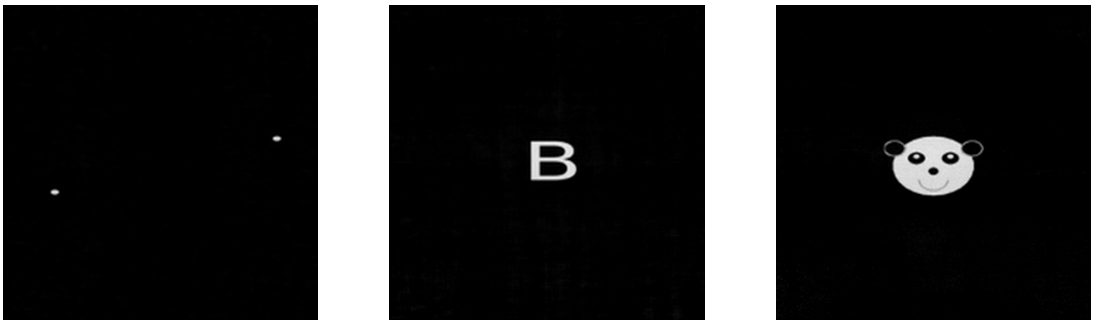


**(a)** *Reconstruction of 2 punctual sources*

**(b)** *Reconstruction of the letter B*

**(c)** *Reconstruction of a simple panda drawing*

**Figure 3.19:** *Gradient Descent reconstruction with simulated raw data*

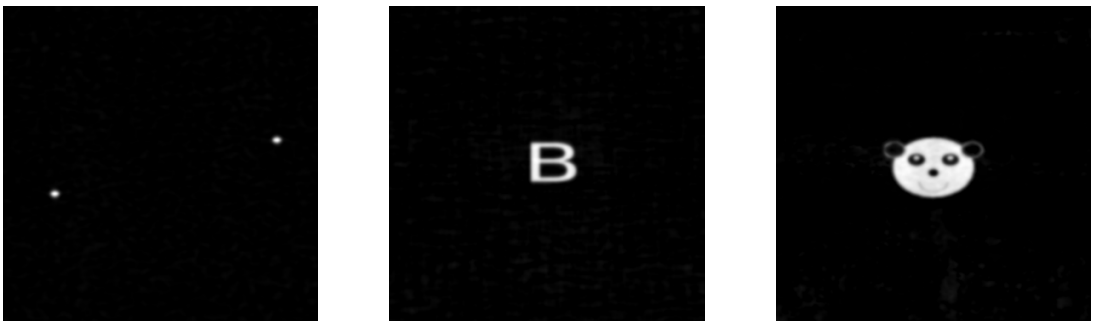


**(a)** *Reconstruction of 2 punctual sources*

**(b)** *Reconstruction of the letter B*

**(c)** *Reconstruction of a simple panda drawing*

**Figure 3.20:** *Alternating Direction Method of Multipliers reconstruction with simulated raw data*

Moreover, to illustrate the potential of the DiffuserCam, the results of image reconstructions using the experimental setup are depicted in Figure 3.21. This confirms the trade-off explained in the calibration part of this chapter, in Subsection 3.1.1, stating that the farther away the source is and the closer the sensor is, both with respect to the diffuser, the smaller the reconstruction image will be.

Tables 3.5 and 3.6 summarize the evaluation results for the obtained reconstructions compared to the original images.

From two punctual sources to the simple panda drawing, the MSE values show a notable increase, highlighting a corresponding increase in reconstruction error for the more complex images. Similarly, PSNR values exhibit a downward trend with increasing image complexity, mirroring a decline in overall reconstruction fidelity. SSIM values,

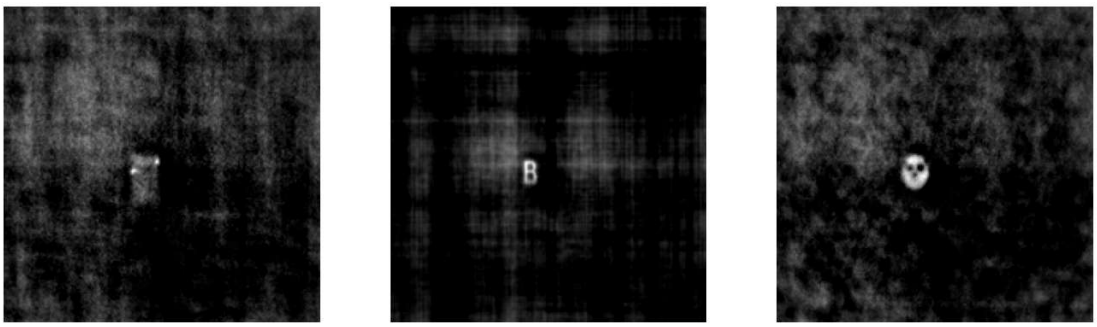

**(a)** *Real reconstruction of 2 punctual sources*

**(b)** *Real reconstruction of the letter B*

**(c)** *Real reconstruction of a simple panda drawing*

**Figure 3.21:** *Real image reconstruction*

| ADMM Simulation Results | MSE | PSNR | SSIM | LPIPS |
|---|---|---|---|---|
| 2 Punctual Sources | 1495.263 | 16.384 | 0.923 | 0.344 |
| Letter B | 2015.967 | 15.086 | 0.849 | 0.356 |
| Simple Panda Drawing | 3176.017 | 13.112 | 0.811 | 0.401 |

**Table 3.5:** *ADMM Simulation Results*

which serve as a gauge for structural similarity, tend to decrease, signaling a less precise reconstruction for more intricate images. Simultaneously, LPIPS values register a rise, implying a perceptual quality that diminishes as image complexity intensifies.

| GD Simulation Results | MSE | PSNR | SSIM | LPIPS |
|---|---|---|---|---|
| 2 Punctual Sources | 1499.424 | 16.372 | 0.847 | 0.415 |
| Letter B | 2122.681 | 14.862 | 0.721 | 0.425 |
| Simple Panda Drawing | 3707.796 | 12.440 | 0.694 | 0.469 |

**Table 3.6:** *GD Simulation Results*

Following a similar pattern to the ADMM results, we observe an increase in SSIM and a decrease in PSNR as image complexity increases. SSIM values, on the other hand, tend to be consistently lower than those obtained by ADMM, suggesting that GD may not be as adept at retaining structural detail. In addition, LPIPS values exceed those obtained by ADMM, implying a perceptual quality that leaves something to be desired in GD reconstructions.

In real-world assessments, MSE values show a significant increase compared to simulations, signaling increased reconstruction errors. Correspondingly, PSNR values show a decrease, indicating reduced reconstruction quality. In particular, SSIM values are noticeably reduced for the letter B and the simple panda drawing, indicating a deterioration in structural fidelity. Additionally, LPIPS values increase significantly,

| GD Real Results | MSE | PSNR | SSIM | LPIPS |
|---|---|---|---|---|
| 2 Punctual Sources | 6003.247 | 10.347 | 0.664 | 0.867 |
| Letter B | 6687.397 | 9.878 | 0.127 | 0.932 |
| Simple Panda Drawing | 8017.002 | 9.091 | 0.108 | 0.914 |

**Table 3.7:** *GD Real Results*

indicating perceptually poor quality in real-world tests.

## 3.4 Conclusion

The DiffuserCam, developed by Laura Waller's team, captures images using a diffuser instead of a conventional lens. The imaging process involves capturing light scattered by the diffuser to form a caustic pattern on the sensor, which is then reconstructed using computational algorithms such as ADMM (Alternating Direction Method of Multipliers) and Gradient Descent (GD). Key steps in this process include calibration, forward modeling, and solving inverse problems using optimization techniques.

Calibration of the DiffuserCam is critical for obtaining accurate image reconstructions. It involves determining the optimal distances between the sensor, diffuser, and light source to achieve the clearest point spread function (PSF). Experiments showed that the best PSF is achieved when the light source is farthest from the diffuser and the sensor is closest to the diffuser. This setup ensures a sharp and narrow PSF, which is essential for high-quality image reconstruction. An aperture is also used to crop the field of view, maintaining a shift-invariant setup that is necessary for the linear superposition model used in the reconstruction algorithms.

Image reconstruction with the DiffuserCam utilizes advanced optimization techniques to solve the inverse problem of recovering the scene from sensor measurements. The algorithms tested include gradient descent and ADMM, each with its own approach to handling the linear convolution model and regularization terms like total variation and sparsity. Simulation results demonstrated that both methods improve in accuracy with an increasing number of iterations, effectively reconstructing various test images such as point sources, letters, and simple drawings. These findings highlight the potential of the DiffuserCam as a versatile and cost-effective solution for lensless imaging applications.

#### Conclusion on the reconstruction algorithms

ADMM appears to perform better than GD in simulated scenarios, particularly in maintaining structural integrity and perceptual quality. However both methods struggle more with complex images (the panda image 3.11c), with higher errors and lower quality metrics. The significant performance drop in real results for GD suggests that

real-world conditions introduce complexities that are not fully captured in simulations. Improvement strategies could include better noise handling, more robust algorithms, or hybrid approaches combining strengths of both ADMM and GD methods. Moreover, the PSF capture might include some physical noise.

# 4

# PolariCam

The name *PolariCam* refers to the combination of polarizing filters with the *DiffuserCam* aiming to create a lensless camera able to characterize a linearly polarized light source in a single-shot.

First, using the background on light polarization described in Section 2.2, the mathematical model adopted to characterize linear polarization is developed. It is then applied to a conventional lens imaging system to verify the accuracy of the results.

Secondly, the physical design of the PolariCam is described in order to obtain a single shot with all the source's polarization information needed to characterize it.

## 4.1 Detection and Mathematical Model

The linear polarization of a source is represented using the Jones formalism [17]. Thanks to this representation, the light's behavior as it propagates through linear polarizer can be expressed and used toward the purpose of our detection model. The Stokes parameters are then used to obtain a comprehensive description of the polarization state of the source.

### 4.1.1 Jones Matrix of a Polarizer

At its core, the Jones matrix represents a linear transformation that relates the state of polarized light before and after it interacts with an optical element. In simpler terms, it tells us how the polarization state of light changes as it passes through the element.

Mathematically, the Jones matrix is a 2x2 complex matrix. Each element of the matrix represents the amplitude and phase change of the two orthogonal components of the electric field vector (denoted as $E_x$ and $E_y$) of the light. These components are aligned with the reference axes of the optical system, the $x$ and $y$ directions, as represented in Figure 4.2.

The Jones matrices for polarizers aligned along the $\hat{x}$ and $\hat{y}$ axes are given by the Jones matrices 4.1 and 4.2

$$/\!/\hat{x} \rightarrow \quad T_0 = \begin{pmatrix} 1 & 0 \\ 0 & 0 \end{pmatrix} \tag{4.1}$$

$$/\!/\hat{y} \rightarrow \quad T_{\frac{\pi}{2}} = \begin{pmatrix} 0 & 0 \\ 0 & 1 \end{pmatrix} \tag{4.2}$$

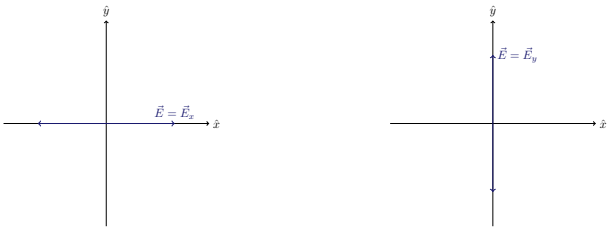


**(a)** *Plane wave propagation oriented with the $\hat{x}$ axis*

**(b)** *Plane wave propagation oriented with the $\hat{y}$ axis*

**Figure 4.1:** *Plane wave propagation through the plane $(x, y)$ aligned with each axis*

A polarizer oriented at angle $\theta$ is aligned with the direction $\hat{e}_\theta$ given by the Jones vector 4.3.

$$/\!/\hat{e}_\theta = \begin{pmatrix} \cos\theta \\ \sin\theta \end{pmatrix} \tag{4.3}$$

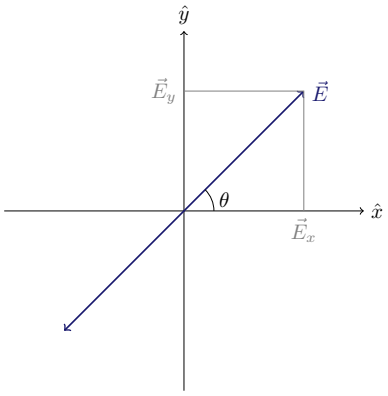


**Figure 4.2:** *Light represented as a plane wave in the $(x, y)$ plane*

For a linear polarizer oriented at an angle $\theta$ from the horizontal $\hat{x}$ axis, the rotation matrix $R_\alpha$ 4.4 is used for computations.

$$R_\alpha = \begin{pmatrix} \cos\alpha & \sin\alpha \\ -\sin\alpha & \cos\alpha \end{pmatrix} \tag{4.4}$$

The Jones matrix of a polarizer oriented at angle $\theta$ is given by expression 4.5.

$$T_\theta = R_\theta^{-1} \cdot T_0 \cdot R_\theta = \hat{e}_\theta \cdot \hat{e}_\theta^T \tag{4.5}$$

This computation yields the following matrix 4.6.

$$T_\theta = \begin{pmatrix} \cos^2\theta & \frac{1}{2}\sin 2\theta \\ \frac{1}{2}\sin 2\theta & \sin^2\theta \end{pmatrix} \tag{4.6}$$

For the specific angles $\frac{\pi}{4}$ and $-\frac{\pi}{4}$, the Jones matrices are respectively matrix 4.7 and matrix 4.8.

$$\theta = \frac{\pi}{4} \rightarrow \quad \hat{e}_{\frac{\pi}{4}} = \begin{pmatrix} \frac{1}{\sqrt{2}} \\ \frac{1}{\sqrt{2}} \end{pmatrix} \rightarrow \quad T_{\frac{\pi}{4}} = \begin{pmatrix} \frac{1}{2} & \frac{1}{2} \\ \frac{1}{2} & \frac{1}{2} \end{pmatrix} \tag{4.7}$$

$$\theta = -\frac{\pi}{4} \rightarrow \quad \hat{e}_{-\frac{\pi}{4}} = \begin{pmatrix} \frac{1}{\sqrt{2}} \\ -\frac{1}{\sqrt{2}} \end{pmatrix} \rightarrow \quad T_{-\frac{\pi}{4}} = \begin{pmatrix} \frac{1}{2} & -\frac{1}{2} \\ -\frac{1}{2} & \frac{1}{2} \end{pmatrix} \tag{4.8}$$

### 4.1.2 Description of Light Propagation Through Polarizers

When polarized light passes through an optical element described by a Jones matrix, such as the analyzer depicted in Figure 4.3, the resulting polarization state can be calculated by multiplying the Jones matrix representing that element with the Jones vector representing the polarization state of the incident light. This multiplication generates a new Jones vector representing the polarization state of the transmitted light.

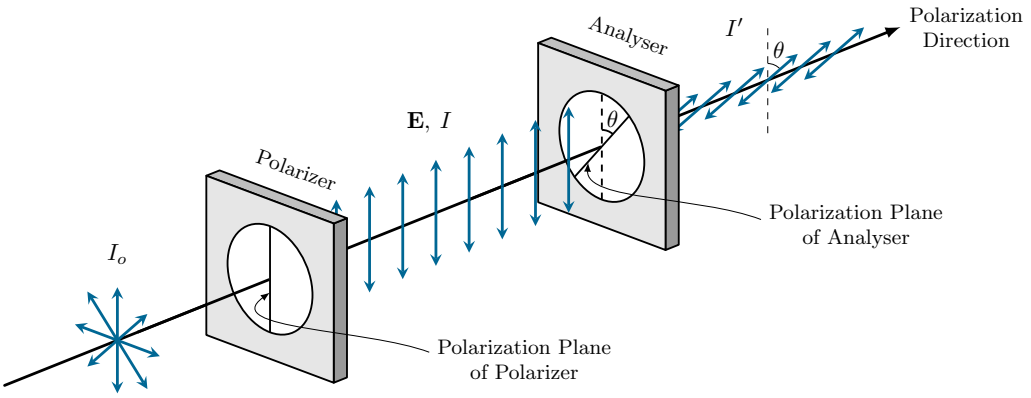


**Figure 4.3:** *Optical elements such as linear polarizers following each other*

Given a plane wave described by the Jones vector

$$\vec{E} = \begin{pmatrix} \alpha \\ \beta \end{pmatrix} = \begin{pmatrix} r \cdot e^{i\rho} \\ s \cdot e^{i\sigma} \end{pmatrix} \tag{4.9}$$

This light is linearly polarized if $\Delta = \rho - \sigma \in \{0, \pi\}$.

After passing through a polarizer $T_\theta$, the plane wave $\vec{E}$ is computed with relation 4.10 and leads to the matrix 4.11.

$$\vec{E}_\theta = \vec{E}^T \cdot T_\theta = \begin{pmatrix} \alpha & \beta \end{pmatrix} \cdot \begin{pmatrix} \cos^2\theta & \frac{1}{2}\sin 2\theta \\ \frac{1}{2}\sin 2\theta & \sin^2\theta \end{pmatrix} \tag{4.10}$$

$$= \begin{pmatrix} \cos\theta \cdot (\alpha\cos\theta + \beta\sin\theta) \\ \sin\theta \cdot (\alpha\cos\theta + \beta\sin\theta) \end{pmatrix} \tag{4.11}$$

If $\vec{E}$ passes through $T_0$, $T_{\frac{\pi}{2}}$, $T_{\frac{\pi}{4}}$, and $T_{-\frac{\pi}{4}}$, the Jones vectors of the light can be written as in expressions 4.12.

$$\vec{E}_0 = \begin{pmatrix} \alpha \\ 0 \end{pmatrix}, \quad \vec{E}_{\frac{\pi}{2}} = \begin{pmatrix} 0 \\ \beta \end{pmatrix}, \quad \vec{E}_{\frac{\pi}{4}} = \begin{pmatrix} \frac{\alpha+\beta}{2} \\ \frac{\alpha+\beta}{2} \end{pmatrix}, \quad \vec{E}_{-\frac{\pi}{4}} = \begin{pmatrix} \frac{\alpha-\beta}{2} \\ -\frac{\alpha-\beta}{2} \end{pmatrix} \tag{4.12}$$

**Intensity of the Light**

The intensity of the light is given by the square norm of the Jones vector, $I = \|\vec{E}\|^2 = E_x^2 + E_y^2$, with $E_x$ and $E_y$ the components of $\vec{E}$ aligned respectively with the axis $\hat{x}$ and $\hat{y}$. Generally, for an arbitrary orientation of the incident light $\theta$, the expression 4.13 is obtained.

$$I_\theta = \|\vec{E}_\theta\|^2 \tag{4.13}$$

$$= (\cos\theta)^2 \cdot |\cos\theta \cdot \alpha + \sin\theta \cdot \beta|^2 + (\sin\theta)^2 \cdot |\cos\theta \cdot \alpha + \sin\theta \cdot \beta|^2 \tag{4.14}$$

$$= |\cos\theta \cdot \alpha + \sin\theta \cdot \beta|^2 = \|(e_\theta^T \cdot v) \cdot e_\theta\|^2 \tag{4.15}$$

Finally, by injecting the complex notation, the general intensity is obtained with expression 4.16.

$$I_\theta = |r\cos\theta + s\sin\theta \cdot e^{-i\Delta}|^2 \tag{4.16}$$

$$= \frac{r^2+s^2}{2} + \frac{\cos 2\theta}{2} \cdot (r^2 - s^2) + r \cdot s \cdot \sin 2\theta \cdot \cos\Delta \tag{4.17}$$

For the specific orientations denoted $x$ ($\theta = 0$), $y$ ($\theta = \frac{\pi}{2}$), $a$ ($\theta = \frac{\pi}{4}$), and $b$ ($\theta = -\frac{\pi}{4}$), the theoretical intensities of the incident light $v$ are gathered in equations 4.18 to 4.21.

$$I_x = \|v_x\|^2 = \alpha^2 = r^2 \tag{4.18}$$
$$I_y = \|v_y\|^2 = \beta^2 = s^2 \tag{4.19}$$
$$I_a = \|v_a\|^2 = \frac{|\alpha+\beta|^2}{2} = \frac{1}{2}(r^2+s^2+2rs\cos\Delta) \tag{4.20}$$
$$I_b = \|v_b\|^2 = \frac{|\alpha-\beta|^2}{2} = \frac{1}{2}(r^2+s^2-2rs\cos\Delta) \tag{4.21}$$

The relation 4.22 is pointed out.

$$I_x + I_y = I_a + I_b = r^2 + s^2 \tag{4.22}$$

**Computation of $\Delta$**

To determine if the light is linearly polarized, the value of the phase shift $\Delta$ between the Jones vector components of the incident lights needs to be either 0 or $\pi$. The combination of the specific intensities computed previously in equations 4.18-4.21, provides an approach to recovering the term $\cos\Delta$. Two methods were gathered in expressions 4.23 and 4.24.

$$R_i = \frac{I_a - I_b}{2\sqrt{I_x I_y}} = \frac{2rs\cdot\cos\Delta}{2rs} = \cos\Delta \tag{4.23}$$

$$R_j = \frac{I_a - \frac{1}{2}(I_x+I_y)}{\sqrt{I_x I_y}} = \frac{rs\cdot\cos\Delta}{rs} = \cos\Delta \tag{4.24}$$

The phase shift $\Delta$ can be recovered, and the characteristic values for linearly polarized light are identified in the following relationships 4.25.

$$\begin{aligned} R = 1 &\iff \Delta = 0 \\ R = -1 &\iff \Delta = \pi \end{aligned} \tag{4.25}$$

In conclusion, if $|R| = 1$, the light is linearly polarized.

### 4.1.3 Stokes parameters

The Stokes parameters are a set of four parameters used to describe the polarization state of light by capturing both the amplitude and phase information of the electric field vector $\vec{E}$ [21].

Mathematically, the four Stokes parameters, $S_0$, $S_1$, $S_2$, and $S_3$, are given by the following expressions 4.26 to 4.29.

$$S_0 = \langle E_x^2 \rangle + \langle E_y^2 \rangle \tag{4.26}$$

$$S_1 = \langle E_x^2 \rangle - \langle E_y^2 \rangle \tag{4.27}$$

$$S_2 = 2\langle E_x E_y \cos\Delta \rangle \tag{4.28}$$

$$S_3 = 2\langle E_x E_y \sin\Delta \rangle \tag{4.29}$$

Where $\langle \cdot \rangle$ denotes the time-average over one period of the light wave, and $\Delta$ is the phase difference between the horizontal and vertical components of $\vec{E}$. The fourth parameter $S_4$ is used to analyze circularly polarized light and will therefore not be used in this development or work.

From the intensities recovered at the specific orientations used (0rad, $\frac{\pi}{2}$rad, $\frac{\pi}{4}$rad, $-\frac{\pi}{4}$rad), the Stokes parameters can be computed as follows in expressions 4.30, 4.31, and 4.32.

$$S_0 = I = I_x + I_y \tag{4.30}$$

$$S_1 = Q = I_x - I_y \tag{4.31}$$

$$S_2 = U = I_a - I_b \tag{4.32}$$

- $I$ is the total intensity of the light transmitted through the polarizer oriented at $\theta = 0°$ and $\theta = \frac{\pi}{2}$rad= 90°.

- $Q$ represents the difference in intensity between light transmitted through polarizers oriented at $\theta = 0°$ and $\theta = \frac{\pi}{2}$rad= 90°. This difference quantifies the degree of linear polarization along the $\hat{x}$ axis.

- $U$ represents the difference in intensity between light transmitted through polarizers oriented at $\theta = \frac{\pi}{4}$rad= 45° and $\theta = -\frac{\pi}{4}$rad= −45°. This difference quantifies the degree of linear polarization along the $/\!/\hat{e}_{\frac{\pi}{4}}$ axis.

By measuring the intensity of light transmitted through each polarizer and performing the Stokes parameters computation, a comprehensive description of the polarization state of the light is provided. The Degree Of Linear polarization (DOLP) and the Angle Of Linear polarization (AOLP) are given with the following formulas 4.33 and 4.34.

$$DOLP = \frac{\sqrt{S_1^2 + S_2^2}}{S_0} \tag{4.33}$$

$$AOLP = \frac{1}{2}\arctan\left(\frac{S_2}{S_1}\right) \tag{4.34}$$

### 4.1.4 Lens observation and detection

To ensure that the linear polarization detection method performs correctly, a camera sensor with a lens is used along with a point light source. A polarizer is precisely oriented in front of the camera using a rotating device. The experimental setup is illustrated in Figure 4.4.

**(a)** *Tool used for precise polarizer orientation*

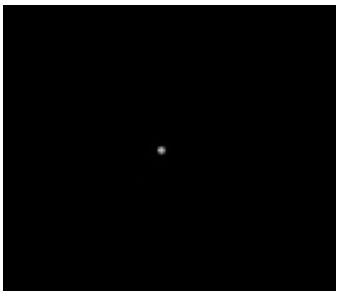

**(b)** *Observed source with lensed camera sensor*

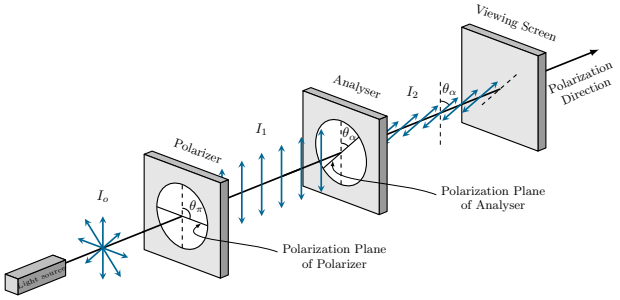


**(c)** *Schematic of the data acquisition for polarization state detection*

**Figure 4.4:** *Observation setup with a lensed camera sensor*

The measured intensities of the light source linearly polarized with $\theta_{\text{source}} \in \{0, 90, 45, -45\}^\circ$ and the polarizing filter in front of the camera as $\theta_{\text{polarizer}} \in \{0, 90, 45, -45\}^\circ$.
As the theoretical expected intensities of the light going through each polarizer are known, as represented by matrix 4.35, the ratios between the measured intensities and expected intensities for all the combinations of filters are computed and stored in the matrix $\Gamma$, 4.36.

$$\text{expected\_intensities} = \begin{bmatrix} I_{x0} & 0 & \frac{I_{x0}}{\sqrt{2}} & \frac{I_{x0}}{\sqrt{2}} \\ 0 & I_{y0} & \frac{I_{y0}}{\sqrt{2}} & \frac{I_{y0}}{\sqrt{2}} \\ \frac{I_{a0}}{2} & \frac{I_{a0}}{2} & I_{a0} & 0 \\ \frac{I_{b0}}{2} & \frac{I_{b0}}{2} & 0 & I_{b0} \end{bmatrix} \tag{4.35}$$

$$\Gamma_{ij} = \frac{\text{measured\_intensities}_{ij}}{\text{expected\_intensities}_{ij}} \tag{4.36}$$

With $i$ the index of the linear source orientation and $j$ the index corresponding to the

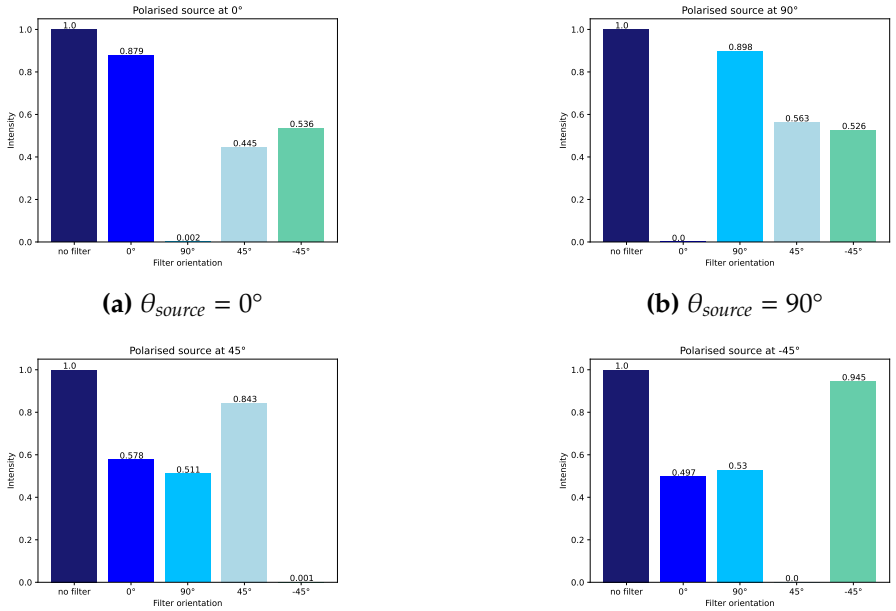


**(a)** $\theta_{source} = 0°$ **(b)** $\theta_{source} = 90°$

**(c)** $\theta_{source} = 45°$ **(d)** $\theta_{source} = 135°$

**Figure 4.5:** *Normalized captured intensities for polarized source and sub-sequence of polarizers in front of sensor*

filter in front of the camera.

This matrix $\Gamma$ allows for identifying the impact of the polarizing filters on the intensity of the incident light. By applying a mean to each column of the matrix, the coefficient corresponding to the intensity attenuation of the light going through the polarizer in front of the camera can be recovered.

Finally, the adjusted intensities are computed by applying the mean attenuation coefficient to each measurements such as in equation 4.37.

$$\text{Adjusted\_intensity}_{ij} = \text{measured\_intensity}_{ij} \times \text{mean}(\Gamma_j) \tag{4.37}$$

Once the intensities are adjusted, the polarization state of the light source can be computed by implementing the formulas of the $R$-coefficient ($R = \cos\Delta$, equation 4.25) and the Stokes parameters (4.30, 4.31, 4.32).

### Evaluation metrics and Results

In summary, the formulas used to characterize the linear polarization state of a light source are the following:

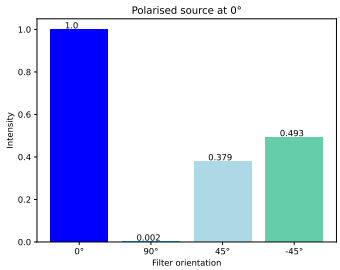


**(a)** $\theta_{source} = 0°$

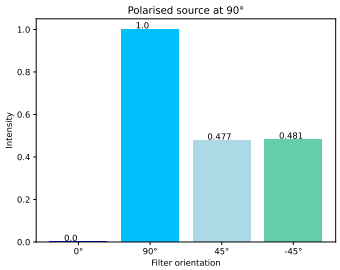


**(b)** $\theta_{source} = 90°$

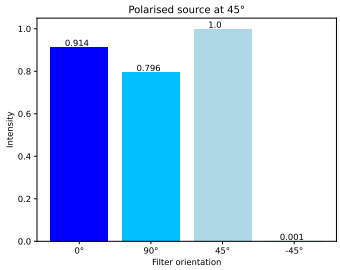


**(c)** $\theta_{source} = 45°$

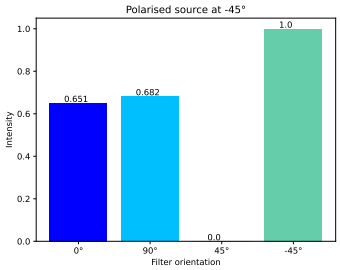


**(d)** $\theta_{source} = 135°$

**Figure 4.6:** *Normalized and corrected captured intensities for polarized source and sub-sequence of polarizers in front of sensor after correct*

$$\begin{aligned} DOLP &= \frac{\sqrt{S_1^2+S_2^2}}{S_0} = \frac{\sqrt{(I_x-I_y)^2+(I_a-I_b)^2}}{I_x+I_y} \\ AOLP &= \frac{1}{2}\arctan\left(\frac{S_2}{S_1}\right) = \frac{1}{2}\arctan\left(\frac{(I_a-I_b)}{(I_x-I_y)}\right) \\ R &= |\cos\Delta| = \left|\frac{I_a-I_b}{2\sqrt{I_xI_y}}\right| \end{aligned} \tag{4.38}$$

To evaluate quantitatively the results obtained, the following metrics are computed [1]:

- **Root Mean Squared Error (RMSE):** the square root of the MSE. It provides a measure of the average magnitude of the error. It is given by:

$$\text{RMSE} = \sqrt{\frac{1}{n}\sum_{i=1}^{n}(y_i - \hat{y}_i)^2} \tag{4.39}$$

- **Mean Absolute Error (MAE):** measures the average magnitude of the errors in a set of predictions without considering their direction. It is given by:

$$\text{MAE} = \frac{1}{n}\sum_{i=1}^{n}|y_i - \hat{y}_i| \tag{4.40}$$

The results obtained from lens detection are provided in Table 4.1
Ideally, both the Degree of Linear Polarization (DOLP) and the R-coefficient should be

| Source | DOLP | AOLP (degrees) | R |
|---|---|---|---|
| **0°** | 1.003 | -3.25 | 0.164 |
| **90°** | 1.000 | 90.13 | 0.955 |
| **45°** | 0.588 | 41.63 | 0.585 |
| **135°** | 0.751 | 134.10 | 0.675 |
| **20°** | 0.741 | 18.45 | 0.552 |

**Table 4.1:** *Polarization Data*

1, indicating perfect linear polarization. However, deviations from these ideal values are observed in various sources. For example, the DOLP values for $\theta_{source} = 0°$ and $\theta_{source} = 90°$ are slightly above 1, suggesting a possible overestimation in the polarization measurements. Similarly, the R values for these sources are significantly different from 1, indicating inaccuracies in the intensities measurements. On the other hand, sources such as $\theta_{source} = 45°$ and $\theta_{source} = 135°$ have DOLP and R values closer to 1, indicating more accurate measurements, although small deviations are still present.

The analysis of the quantitative evaluation of polarization data, as defined in Tables 4.2, 4.3 provides insights into the characteristics of incident light and the performance of the measurement system.

| Metric | RMSE | MAE |
|---|---|---|
| **DOLP** | 0.2447 | 0.1848 |
| **AOLP** | 2.2405 | 1.8381 |
| **R** | 0.4856 | 0.4138 |

**Table 4.2:** *Error Metrics for DOLP, AOLP, and R*

The Root Mean Squared Error (RMSE) and Mean Absolute Error (MAE) for DOLP indicate a moderate level of deviation from the ideal DOLP value of 1. This suggests that while the camera's measurements are reasonably accurate, there are noticeable discrepancies that need to be addressed. For the AOLP, the substantial errors revealed by the RMSE and MAE indicate significant inaccuracies in the angle measurements, which could impact the overall accuracy of polarization measurements.

Examining the R-coefficient, which serves as another descriptor of the DOLP, the error metrics reflect moderate deviations from the expected value of 1. While the R-coefficient measurements are relatively accurate, the presence of significant errors indicates that there may be systematic issues in how the R-coefficient is derived or measured. The higher errors for the R-coefficient compared to DOLP suggest that it might be more sensitive to measurement inaccuracies.

| Uncertainty Metric | RMSE | MAE |
|---|---|---|
| **DOLP** | 0.0621 | 0.0721 |
| **AOLP** | 0.5406 | 0.5867 |
| **R** | 0.1155 | 0.1155 |

**Table 4.3:** *Uncertainty Metrics for DOLP, AOLP, and R*

The uncertainty metrics provide some indication about the precision of these measurements. For the DOLP, the low RMSE and MAE values suggest that the measurements are consistently close to the true value, despite the moderate overall error. However, the uncertainties for the AOLP indicate significant variability and potential problems with the precision of the angle measurements. For the R-coefficient, the uncertainty metrics suggest that although the measurements are relatively accurate, the moderate errors observed indicate the need for improved measurement techniques or calibration procedures to improve the accuracy and consistency of the description of the DOLP by the R-coefficient.

## 4.2 Setup with DiffuserCam

Using the DiffuserCam for the proposed implementation allows for working with a single-shot image combining the four filters observations instead of having to take four sequential images with the four different filters.

In order for the sensor to capture the four polarizers influence on the incident light, the four filters are designed to fit the sensor size in a *checkerboard-like* as depicted in Figure 4.7.

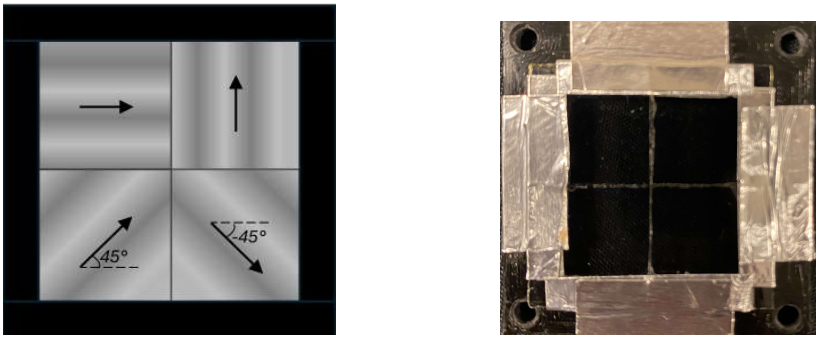


**(a)** *Schematic of the filters in the checkerboard design*

**(b)** *Filters design for the DiffuserCam*

**Figure 4.7:** *Checkerboard design of the filters for the DiffuserCam*

The combination of the DiffuserCam and the filters results in light being diffused through each of the four filters, which are arranged in a large square composed of four smaller subsquares, each with a different orientation. The sensor detects varying

intensities influenced by these distinct filter orientations. Consequently, the intensities recovered in each corner of the captured image correspond to the specific orientation and characteristics of each filter. The splited view of the denoted PolariCam (combination of polarizers with the DiffuserCam) is represented in Figure 4.8.

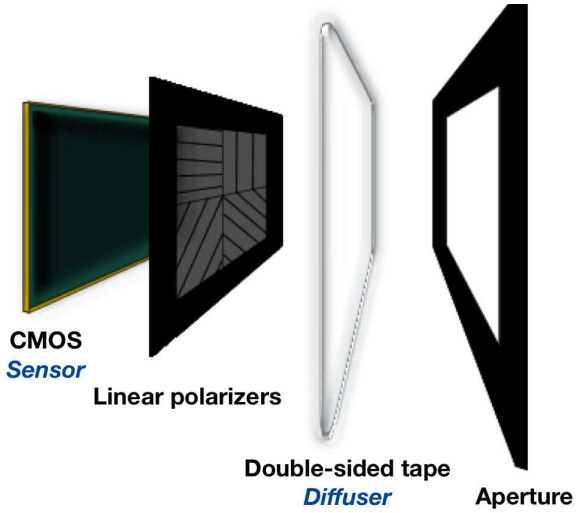


**Figure 4.8:** *PolariCam model - exploded view*

Due to the design of the filter layer in front of the sensor, the recovered image is the result of the superposition of the images produced by each filter in conjunction with the diffuser.

The mathematical formula to express the forward model is written in expression 4.41, with $b$ the captured signal, $v_i$ the incident light signal porpagated through each filter with the respective PSF $h_i$.

$$b = \sum_{i=1}^{4} h_i * v_i = \sum_{i=1}^{4} A_i v_i \tag{4.41}$$

Where each $A_i$ corresponds to the convolution operation with $h_i$, represented in matrix form.

### 4.2.1 PSF calibration

The checkerboard design allows four different PSF to be obtained for the light passing through each of the four filters. These distinct PSF can be recovered by dividing the total captured PSF into four regions. Therefore, for the image reconstruction, the raw captured data will go through the reconstruction algorithms using each distinct PSF on the image. This will result in four distinct reconstructions showing the behavior of the scene seen through each of the filters. The sum of these four different reconstructions will give the final reconstruction of the original image using the concept of superposition, as the assumption of a shift-invariant system is still valid.

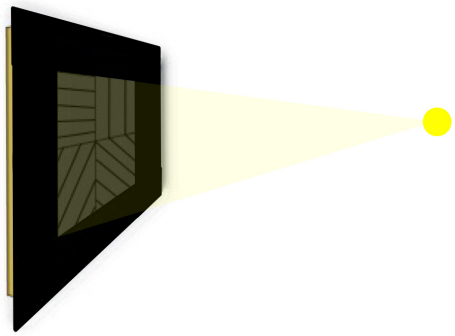

**Figure 4.9:** *PolariCam - calibration*

The PSFs captured were evaluated in the same way as it was evaluated for the DiffuserCam, in Section 3.1. The result of the evaluation with the auto-correlation of the PSF and its cross-section is illustrated in Figure 4.10.

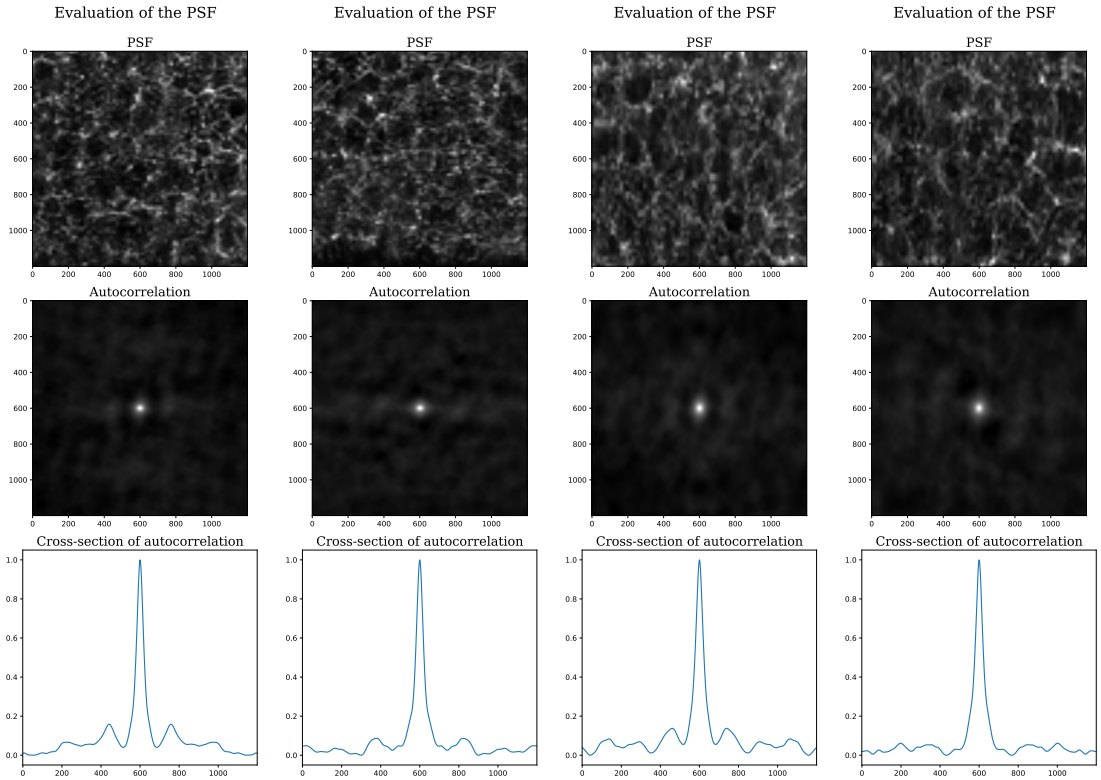


**(a)** $\theta_{polarizer} = 0°$ **(b)** $\theta_{polarizer} = 90°$ **(c)** $\theta_{polarizer} = 45°$ **(d)** $\theta_{polarizer} = 135°$

**Figure 4.10:** *Cropped zones of the polarization-dependant PSF - Autocorrelation evaluation*

To address potential manipulation errors in the orientation of the filters inside the design, the intensities of a linear polarized source were captured with the PolariCam. The light source is polarized with orientations ranging from $\theta_{source} = -90°$ to $\theta_{source} = 90°$, with steps of 2°. The fitted curves of those measurements are depicted in Figure 4.11.

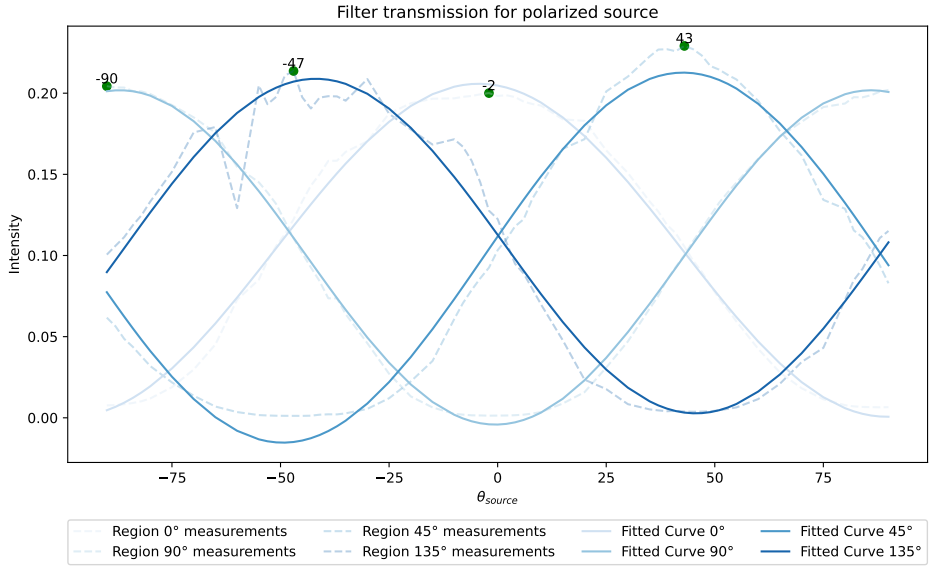


**Figure 4.11:** *Intensity curves of linearly polarized light transmission through the PolariCam*

The orientations of the four filters in the PolariCam are $\theta_{polarizer} = \{-90°; -47°; -2°; 43°\}$. These angles were evaluated by recovering the maximal intensity from the distribution. The orientation error resulting from manual manipulations is two degrees, except for $\theta_{source} = 90° \longrightarrow -90°$, which is the same in terms of linear polarization.

## 4.3 Reconstruction algorithm

Since the signal $Av$ is the sum of four PSFs convolved with their respective signals, the equations for both Gradient Descent (GD) and Alternating Direction Method of Multipliers (ADMM) used for the DiffuserCam will need to be adjusted accordingly.

### 4.3.1 Key modifications

- **Multiple PSFs**: Each signal $v_i$ is convolved with its respective PSF $h_i$, leading to multiple $A_i$ matrices.
- **Separate Gradients and Updates**: Each signal $v_i$ has its own gradient and update rules, considering the contributions from all four PSFs.
- **Combined Objective Function**: The optimization function takes into account the sum of all convolved signals.
- **Augmented Lagrangian with Multiple Terms**: The Lagrangian formulation includes terms for all signals and their respective constraints.

For the GD algorithm:

$$g(v) = \frac{1}{2}\| \sum_{i=1}^{4} A_i v_i - b\|_2^2 \tag{4.42}$$

$$\nabla_{v_i} g(v) = A_i^H \left( \sum_{i=1}^{4} A_i v_i - b \right) \tag{4.43}$$

For the ADMM algorithm:

$$\hat{v} = \arg \min_{v_1, v_2, v_3, v_4 \geq 0} \frac{1}{2} \left\| b - \sum_{i=1}^{4} A_i v_i \right\|_2^2 + \lambda \sum_{i=1}^{4} \|u_i\|_1$$

This adaptation ensures that the reconstruction algorithm correctly accounts for the combined effect of the four PSFs and their respective regions in the captured image.

# 5

# Results and Discussion

The PolariCam is designed in order to retreive the polarization state of a light source coming from a scene in a single shot. Using the Jones formalism and the Stokes parameters, the mathematical model developed in Section 4.1 is tested on DiffuserCam captured images in this chapter.

## 5.1 Experimental Setup

Precise alignment ensured that the four linear polarizers, arranged in a checkerboard pattern in the DiffuserCam aperture, were correctly oriented. This configuration allowed simultaneous image capture through each polarizer, enabling complete data acquisition in a single shot.

Moreover, once the light has been identified as linearly polarized, its orientation can be deduced using Stokes parameter analysis. This analytical approach provides valuable information on the polarization characteristics of the captured light, enhancing our understanding of the scene under study.

Images of a simple light source were captured at different polarizer angles: 0°, 45°, 90°, and 135°. Each set of images was processed to compute the Stokes parameters ($S_0$, $S_1$, $S_2$).

## 5.2 Quantitative Analysis

The quantitative analysis involved measuring the accuracy and precision of the polarization detection. Table 5.1 summarizes the accuracy of the reconstructed polarization angles compared to known reference angles.

#### Source Polarization Parameters

The analysis of source polarization parameters, as presented in Table 5.1, reveals distinct characteristics of polarized and non-polarized light sources. Notably, polarized sources

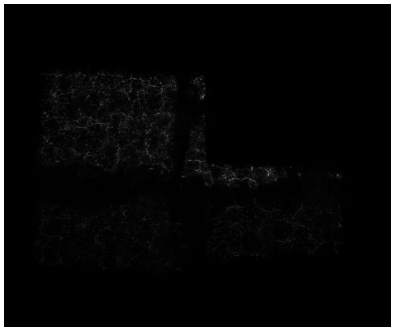

**(a)** $\theta_{source} = 0°$

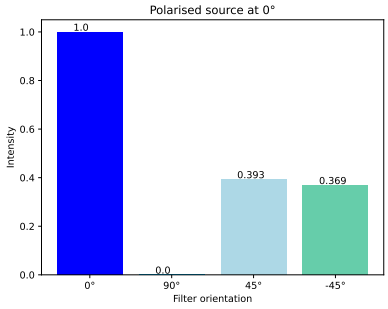


**(b)** $\theta_{source} = 0°$

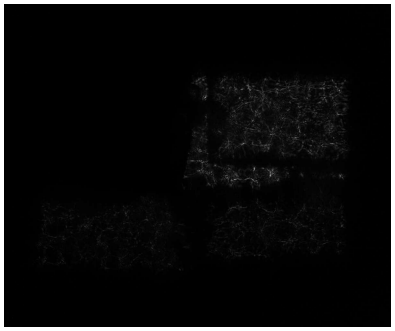

**(c)** $\theta_{source} = 90°$

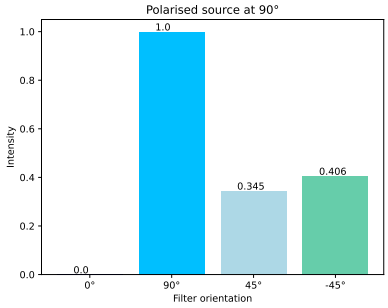


**(d)** $\theta_{source} = 90°$

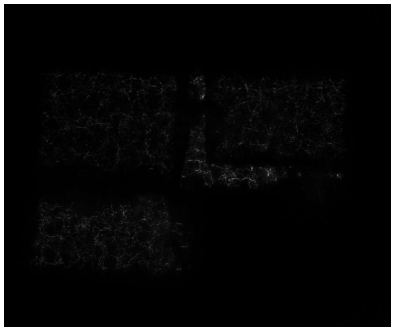

**(e)** $\theta_{source} = 45°$

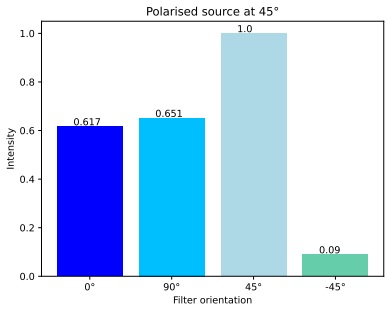


**(f)** $\theta_{source} = 45°$

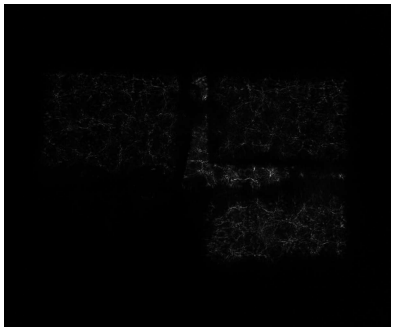

**(g)** $\theta_{source} = 135°$

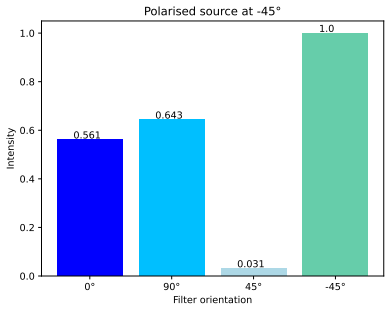


**(h)** $\theta_{source} = 135°$

**Figure 5.1:** *Sample raw images captured at polarizer angles of 0°, 45°, 90°, and 135° and their respective intensities*

exhibit varying degrees of linear polarization (DOLP), ranging from approximately 1.000 to 0.718. Additionally, the angle of linear polarization (AOLP) varies significantly among the sources, spanning from 0.688° to 135.532°. The $R$-coefficient, indicative

| Source | R | DOLP | AOLP (degrees) |
|---|---|---|---|
| **0** | 1.548 | 1.000 | 0.688 |
| **90** | 1.575 | 1.002 | 91.938 |
| **45** | 0.718 | 0.718 | 42.949 |
| **135** | 0.723 | 0.807 | 135.532 |
| **65** | 0.693 | 0.847 | 69.567 |
| **Nonpolarized** | 0.042 | 0.051 | Ø |

**Table 5.1:** *Polarization of PolariCam measurements*

of phase coherence and polarization characteristics, shows a wide range of values, reflecting differences in the degree of polarization among the sources. Conversely, the non-polarized source demonstrates minimal polarization characteristics, with significantly lower DOLP and *R* values, underlining its unpolarized nature.

### Error Metrics

| Parameter | RMSE | MAE |
|---|---|---|
| **DOLP** | 0.171 | 0.119 |
| **AOLP** | 0.004 | 0.004 |
| **R** | 0.443 | 0.420 |

**Table 5.2:** *Error Metrics of PolariCam measurements*

Concerning the error measurements shown in Table 5.2, we observe evaluations of Root Mean Square Error (RMSE) and Mean Absolute Error (MAE) for DOLP, AOLP and the *R* coefficient. These measurements provide an insight into the accuracy and precision of polarization measurements. In particular, the DOLP and AOLP measurements show relatively low error values for all measurements, indicating an accurate estimation of the linear polarization parameters. Conversely, the *R* coefficient estimate shows higher error values, indicating greater uncertainty in the determination of polarization properties.

### Uncertainty Metrics

| Parameter | RMSE | MAE |
|---|---|---|
| **DOLP** | 0.059 | 0.061 |
| **AOLP** | 0.001 | 0.001 |
| **R** | 0.068 | 0.069 |

**Table 5.3:** *Uncertainty Metrics of PolariCam measurements*

The uncertainty metrics presented in Table 5.3 quantify the uncertainty associated with the polarization measurements. The RMSE and MAE values for DOLP, AOLP, and the $R$-coefficient provide insights into the reliability and stability of the measurement process. While the uncertainty metrics for DOLP and AOLP indicate moderate levels of uncertainty, higher error values are observed for the $R$-coefficient estimation, suggesting increased uncertainty for this detection method. These findings support the importance of considering error and uncertainty in polarization measurements and motivate further research to improve measurement techniques and reduce uncertainty in polarization analysis.

## 5.3 Reconstructed Images

Using the four different PSF recovered from calibration, the captured image of a light source can be reconstructed through each polarizer with $\theta_{polarizer} \in [0, 90, 45, 135]°$, their angle of polarization. The results are depicted in Figures 5.2, 5.3, 5.4, 5.5.

**(a)** $\theta_{polarizer} = 0°$ **(b)** $\theta_{polarizer} = 90°$ **(c)** $\theta_{polarizer} = 45°$ **(d)** $\theta_{polarizer} = 135°$

**Figure 5.2:** *Reconstructed light source oriented at* 0°

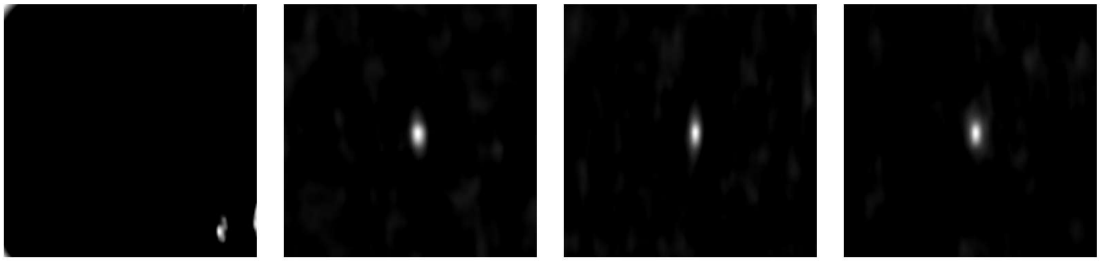

**(a)** $\theta_{polarizer} = 0°$ **(b)** $\theta_{polarizer} = 90°$ **(c)** $\theta_{polarizer} = 45°$ **(d)** $\theta_{polarizer} = 135°$

**Figure 5.3:** *Reconstructed light source oriented at* 90°

## 5.4 Discussion of Findings

The PolariCam system proved effective in detecting linear polarization with reasonable accuracy. The simplicity of the setup and the flexibility in polarizer integration make it a promising tool.

**(a)** $\theta_{polarizer} = 0°$ **(b)** $\theta_{polarizer} = 90°$ **(c)** $\theta_{polarizer} = 45°$ **(d)** $\theta_{polarizer} = 135°$

**Figure 5.4:** *Reconstructed light source oriented at* 45°

**(a)** $\theta_{polarizer} = 0°$ **(b)** $\theta_{polarizer} = 90°$ **(c)** $\theta_{polarizer} = 45°$ **(d)** $\theta_{polarizer} = 135°$

**Figure 5.5:** *Reconstructed light source oriented at* 135°

## 5.5 Future Directions

Future research should explore the reconstruction of images using the Jones vector as the incident signal. This could provide a more complete reconstruction algorithm to better detect the light polarization of more complex sources. The Jones vectors, along with the Stokes parameters to obtain the polarization state of multiple sources in a single shot, can be used to enhance image reconstruction. Additionally, expanding the system to detect circular polarization could provide a more comprehensive analysis of light properties.

# 6

# Conclusion

The integration of linear polarizers into the DiffuserCam system represents a significant advance in polarization detection and imaging technology. Through this research, we have successfully demonstrated the ability to capture and analyze linear light polarization in a single shot, providing a more compact, cost-effective and versatile solution compared to existing methods. The experimental results confirm the effectiveness of the integrated system. The modified DiffuserCam has been shown to detect and reconstruct the polarization state of light from a punctual light source, providing detailed insights into the orientation and degree of polarization.

However, this research also opens up new directions for further study. An intriguing development for future work is the reconstruction of more complex scenes using the Stokes parameters to recover comprehensive polarization information. This would require the development of more sophisticated computational algorithms to handle the increased complexity of real-world scenarios where light interacts with multiple surfaces and media. By addressing these challenges, we can further enhance the ability of the DiffuserCam system to capture detailed and nuanced polarization data, even in complex environments.

In addition, future research could explore the integration of circular polarizers and the analysis of circular polarization components, further extending the versatility of the system.

Investigating the potential of real-time polarization imaging and applying machine learning algorithms to improve the interpretation of polarization data are also promising areas of development.

By advancing our ability to detect and analyze light polarization with a compact and adaptable system, we are contributing to the development of more efficient and versatile imaging solutions.

# Bibliography


[1] S. Acharya. "What are RMSE and MAE?" Medium. (Jun. 15, 2021), [Online]. Available: https://towardsdatascience.com/what-are-rmse-and-mae-e405ce230383.

[2] "Adhésif double face transparent repositionnable et sans trace pour fixation," Lima Adhésifs. (), [Online]. Available: https://www.lima.fr/nos-solutions-adhesives/griptout-double-face-transparent-repositionnable-sans-trace/.

[3] N. Antipa, G. Kuo, R. Heckel, *et al.*, "DiffuserCam: Lensless single-exposure 3d imaging," *Optica*, vol. 5, no. 1, pp. 1–9, 2018. DOI: https://doi.org/10.1364/OPTICA.5.000001.

[4] M. S. Asif, A. Ayremlou, A. Sankaranarayanan, A. Veeraraghavan, and R. G. Baraniuk, "FlatCam: Thin, lensless cameras using coded aperture and computation," *IEEE Transactions on Computational Imaging*, vol. 3, no. 3, pp. 384–397, Sep. 2017, ISSN: 2333-9403, 2334-0118. DOI: 10.1109/TCI.2016.2593662. [Online]. Available: http://ieeexplore.ieee.org/document/7517296/.

[5] N. Badt and O. Katz, "Real-time holographic lensless micro-endoscopy through flexible fibers via fiber bundle distal holography," *Nature Communications*, vol. 13, no. 1, p. 6055, Oct. 13, 2022, Publisher: Nature Publishing Group, ISSN: 2041-1723. DOI: 10.1038/s41467-022-33462-y. [Online]. Available: https://www.nature.com/articles/s41467-022-33462-y.

[6] N. Baek, Y. Lee, T. Kim, J. Jung, and L. Seung Ah, "Lensless polarization camera for single-shot full-stokes imaging," *APL Photonics*, vol. 7, Nov. 1, 2022. DOI: 10.1063/5.0120465.

[7] E. Bezzam. "Evaluating lensless imaging reconstructions," Medium. (Dec. 29, 2022), [Online]. Available: https://medium.com/@bezzam/image-similarity-metrics-applied-to-diffusercam-21998967af8d.

[8] C. Biscarrat, S. Parthasarathy, N. Antipa, G. Kuo, and L. Waller, "Diffuser cam: Lensless imaging algorithms,"

[9] C. Biscarrat, S. Parthasarathy, N. Antipa, G. Kuo, and L. Waller, "How to build a (pi) DiffuserCam,"

[10] V. Boominathan, J. T. Robinson, L. Waller, and A. Veeraraghavan, "Recent advances in lensless imaging," *Optica*, vol. 9, no. 1, pp. 1–16, Jan. 20, 2022, Publisher: Optica Publishing Group, ISSN: 2334-2536. DOI: 10.1364/OPTICA.431361. [Online]. Available: https://opg.optica.org/optica/abstract.cfm?uri=optica-9-1-1.

[11] S. Boyd, "Distributed optimization and statistical learning via the alternating direction method of multipliers," *Foundations and Trends® in Machine Learning*, vol. 3, no. 1, pp. 1–

122, 2010, ISSN: 1935-8237, 1935-8245. DOI: 10.1561/2200000016. [Online]. Available: http://www.nowpublishers.com/article/Details/MAL-016.

[12] "Camera - raspberry pi documentation." (), [Online]. Available: https://www.raspberrypi.com/documentation/accessories/camera.html.

[13] *Full width at half maximum*, in *Wikipedia*, Page Version ID: 1221497442, Apr. 30, 2024. [Online]. Available: https://en.wikipedia.org/w/index.php?title=Full_width_at_half_maximum&oldid=1221497442.

[14] M. Gormley, "Lecture 8: Convergence of gradient descent,"

[15] C. He, H. He, J. Chang, B. Chen, H. Ma, and M. J. Booth, "Polarisation optics for biomedical and clinical applications: A review," *Light: Science & Applications*, vol. 10, no. 1, p. 194, Sep. 22, 2021, Publisher: Nature Publishing Group, ISSN: 2047-7538. DOI: 10.1038/s41377-021-00639-x. [Online]. Available: https://www.nature.com/articles/s41377-021-00639-x.

[16] Jesse K. Adams, Vivek Boominathan, Benjamin W. Avants, *et al.* "Single-frame 3d fluorescence microscopy with ultraminiature lensless FlatScope." (), [Online]. Available: https://www.science.org/doi/10.1126/sciadv.1701548.

[17] "Jones vector representation of polarization states," Fosco Connect. (), [Online]. Available: https://www.fiberoptics4sale.com/blogs/wave-optics/102087110-jones-vector-representation-of-polarization-states.

[18] X. Li, Y. Han, H. Wang, T. Liu, S.-C. Chen, and H. Hu, "Polarimetric imaging through scattering media: A review," *Frontiers in Physics*, vol. 10, Mar. 18, 2022, Publisher: Frontiers, ISSN: 2296-424X. DOI: 10.3389/fphy.2022.815296. [Online]. Available: https://www.frontiersin.org/articles/10.3389/fphy.2022.815296.

[19] Y.-H. Lin, H.-H. Huang, Y.-J. Wang, H.-A. Hsieh, and P.-L. Chen, "Image-based polarization detection and material recognition," *Optics Express*, vol. 30, no. 22, p. 39 234, Oct. 24, 2022, ISSN: 1094-4087. DOI: 10.1364/OE.463332. [Online]. Available: https://opg.optica.org/abstract.cfm?URI=oe-30-22-39234.

[20] K. Monakhova, J. Yurtsever, G. Kuo, N. Antipa, K. Yanny, and L. Waller, "Learned reconstructions for practical mask-based lensless imaging," *Optics Express*, vol. 27, no. 20, p. 28 075, Sep. 30, 2019, ISSN: 1094-4087. DOI: 10.1364/OE.27.028075. arXiv: 1908.11502[cs,eess]. [Online]. Available: http://arxiv.org/abs/1908.11502.

[21] J. Peatross and M. Ware, "Physics of light and optics (black & white)," in Lulu.com, Ed., Section: 6, 2015.

[22] "PI CAMERA MODULE V2.1 | Raspberry Pi Caméra Raspberry Pi v2.1 | Distrelec Belgique," Distrelec Belgium. (), [Online]. Available: https://www.distrelec.be/fr/camera-raspberry-pi-v2-raspberry-pi-pi-camera-module-v2/p/30134462.

[23] Y. Su, C. Yang, Y. Peng, *et al.*, "Lensless shadow microscopy-based shortcut analysis strategy for fast quantification of microplastic fibers released to water," *Water Research*, vol. 258, p. 121 758, Jul. 1, 2024, ISSN: 0043-1354. DOI: 10.1016/j.watres.2024.121758. [Online]. Available: https://www.sciencedirect.com/science/article/pii/S0043135424006596.

[24] J. Tan, L. Niu, J. K. Adams, *et al.*, "Face detection and verification using lensless cameras," *IEEE Transactions on Computational Imaging*, vol. 5, no. 2, pp. 180–194, Jun. 2019, Conference Name: IEEE Transactions on Computational Imaging, ISSN: 2333-9403. DOI: 10.1109/TCI.2018.2889933. [Online]. Available: https://ieeexplore.ieee.org/document/8590781.

[25] A. Tbakhi and S. S. Amr, "Ibn al-haytham: Father of modern optics," *Annals of Saudi Medicine*, vol. 27, no. 6, pp. 464–467, 2007, ISSN: 0256-4947. DOI: 10.5144/0256-4947.2007.464. [Online]. Available: https://www.ncbi.nlm.nih.gov/pmc/articles/PMC6074172/.

[26] "Who invented the first camera?" WorldAtlas. Section: WorldAtlas Originals. (May 17, 2018), [Online]. Available: https://www.worldatlas.com/articles/who-invented-the-first-camera.html.

[27] J. Zhao and M. Li, "Lensless ultrafast optical imaging," *Light: Science & Applications*, vol. 11, no. 1, p. 97, Apr. 18, 2022, ISSN: 2047-7538. DOI: 10.1038/s41377-022-00789-6. [Online]. Available: https://www.nature.com/articles/s41377-022-00789-6.

[28] Y. Zheng, Y. Hua, A. C. Sankaranarayanan, and M. S. Asif, "A simple framework for 3d lensless imaging with programmable masks," in *2021 IEEE/CVF International Conference on Computer Vision (ICCV)*, ISSN: 2380-7504, Oct. 2021, pp. 2583–2592. DOI: 10.1109/ICCV48922.2021.00260. [Online]. Available: https://ieeexplore.ieee.org/document/9710788.

**UNIVERSITÉ CATHOLIQUE DE LOUVAIN**
**École polytechnique de Louvain**
Rue Archimède, 1 bte L6.11.01, 1348 Louvain-la-Neuve, Belgique | **www.uclouvain.be/epl**